ABSTRACT

Title of dissertation: BEAM HALO CREATION AND PROPAGATION IN THE UNIVERSITY OF MARYLAND ELECTRON RING

Christos F. Papadopoulos, Doctor of Philosophy, 2009

Dissertation directed by: Professor Patrick O'Shea
Co-chair: Professor Rami Kishek

In this thesis we discuss the phenomenon of halo creation in charged particle beams. For this, we combine analytical, numerical and experimental work, which focuses on the University of Maryland Electron Ring, but is applicable to a wide range of accelerators in the same intensity regime.

We find that the details of the beam distribution do not affect the structure of the halo, but are nonetheless important as they determine the number of particles in the halo and whether the latter can be regenerated. Furthermore, we show that the halo in configuration and velocity space comprises of the same particles, a prediction that has great importance for halo removal and diagnostics. In particular, we show that even in the case of ideal halo removal in phase space, the complicated internal dynamics of the beam core lead to halo regeneration.

Following on previous work, we construct a theoretical particle-core model that includes skew quadrupoles and compare our results to simulations and experiments. The agreement between these approaches is satisfactory, within the constraints of each case.

BEAM HALO CREATION AND PROPAGATION IN THE UNIVERSITY OF MARYLAND ELECTRON RING

by

Christos F. Papadopoulos

Dissertation submitted to the Faculty of the Graduate School of the
University of Maryland, College Park in partial fulfilment
of the requirements for the degree of
Doctor of Philosophy
2009

Advisory Committee:
Professor Patrick O'Shea, Chair/Advisor
Professor Rami Kishek, Co-Advisor
Professor Richard Ellis
Professor Bill Dorland
Professor Adil Hassam
Professor Victor Granatstein: Dean's Representative

Dedication

Στους γονείς μου, Ιφιγένεια και Φραντζή.

Και σε όσους δεν πρόλαβα να αποχαιρετίσω.

Acknowledgments

I would like first to acknowledge the help and support of my advisors, Professors Rami Kishek and Patrick O'Shea. Their guidance during my years in the UMER group was crucial for shaping my research. Professor Martin Reiser's valuable insights were also important in shaping my intuition on the physics of intense beams.

Along with Prof. Kishek, Dr. Irving Haber was my mentor for all things related to WARP as well as the underlying physical phenomena. Without his deep insight of the physical processes, identifying the important questions would be a lot harder.

The members of the UMER group were extremely helpful, providing both support for conducting the experiments and their valuable insight in the phenomena of intense beam physics. I would particularly like to acknowledge the help of Brian Beaudoin, Dr. Santiago Bernal and Dr. Mark Walter. Dr. David Sutter, Dr. Donald Feldman, Dr. Massimo Cornacchia, Dr. Karen Fiuza and Dr. Terry Godlove were also generous with their time and advice on different aspects of particle beam theory and technology.

Students and graduates of the group, namely Dr. Kai Tian, Dr. Jayankar Thangaraj, Dr. Chao Wu and Eric Voorhies were also helpful in the day to day research and operation of the machine. Gang Bai and Hao Zhang in particular were kind enough to help with conducting the experiments.

I would also like to thank my officemate Dr. Diktys Stratakis whose work on tomography provided valuable insights for the halo creation mechanisms and the complicated phase space dynamics exhibited in beams. Dr. Ralph Fiorito, Dr. Anatoly Shkvarunets and Michael Holloway, whose novel approach on halo diagnostics and in particular the

Optical Transition Radiation method provided the springboard to study the distribution of halo in phase space, a question overlooked in the past.

Simulating the particle beams to great accuracy would have been almost impossible without the PIC code WARP, developed at Lawrence Livermore National Lab. The developers of WARP Dr. David Grote, Dr. Alex Friedman, Dr. Jean-Luc Vay and Dr. Steven Lund have indeed provided the beam physics community with an excellent simulation tool.

As I presented my ongoing research in conferences, the input of experts such as Dr. Tom Wangler, Dr. John Barnard, Mikhail Dorf, Dr. Christopher K. Allen, Dr. Massanori Ikegami, Dr. Jean-Michel Lagniel, Dr. Giuliano Franchetti, Dr. Ingo Hoffman and Dr. Alexei Fedotov was of great value to me, since they pointed out both the previous work on the subject as well as new directions of research.

The opinions expressed in this dissertation are my own and do not necessarily reflect the opinions of any of the above mentioned people. I bear the responsibility for typographical or other errors, and the appropriate credit has been given when referencing the work of others.

Finally, I am obliged to my parents, Ifigeneia and Frantzis Papadopoulos, for providing support during my years as a student. Without them, none of this would not have been possible.

Contents

1.

List of Figures

List of Symbols and Abbreviations

c	the speed of light in vacuum
β	relativistic beta factor: $\beta = v/c$
γ	relativistic gamma factor: $\gamma = (1 - \beta^2)^{-1/2}$
ϵ	beam emittance
K	beam perveance
χ	intensity parameter
IREAP	Institute for Research in Electronics and Applied Physics
UMER	University of Maryland Electron Ring
PDF	Particle Distribution Function
PIC code	Particle in Cell code
FODO lattice	Alternating Gradient Lattice
BPM	Beam position monitor
Q1-6	Injector Quadrupole 1-6
QR1-34	Ring Quadrupole 1-34
RC1-17	Ring diagnostic Chamber 1-17
linac	Linear Accelerator
KV	Kapchinsky-Vladimirsky distribution function
WB	waterbag distribution function
TE	Thermal Equilibrium distribution function
SG	semi-gaussian distribution function

For surely the atoms did not hold council, assigning order to each, flexing their keen minds with questions of place and motion and who goes where.

But shuffled and jumbled in many ways, in the course of endless time they are buffeted, driven along, chancing upon all motions, combinations.

At last they fall into such an arrangement as would create this universe.

Lucretius

Chapter 1

Introduction

1.1 Charged Particle Beams

Particle accelerators are known to the educated public because of the big, celebrated and sometimes unjustly feared colliders [4, 5, 6, 7]. They are used for high energy physics experiments and have greatly advanced our knowledge of elementary particle physics, in addition to having significant side contributions to the advancement of technology, such as the World Wide Web.

In addition to these famous machines, there exists a more diverse group of accelerators, that are more numerous and cover a wide range of energies, sizes and applications [8, 9]. A non-exhaustive list of the latter includes cancer therapy [10], various light sources [11, 12], Free Electron Lasers [13, 14] and neutron sources [15, 16] used to diag-

nose matter at very short length as well as time scales. Future applications may include national defense [17] as well as potential drivers for inertial fusion [18].

For these applications, the goal is to not only accelerate particles to high energy, but also to accelerate as many particles as possible while maintaining good beam quality, meaning **small beam size** and **small velocity spread** of the particles. The requirement of a compact phase space is based on both technical grounds, as a more localized beam allows better control of the particle interactions, as well as on cost, since a larger beam size will, in general, lead to larger magnets, pipes and other parts of the accelerator.

Increasing intensity poses a significant challenge, since in the vast majority of cases the particles being accelerated belong to the same species and are charged, hence repelling each other. Thus, adding more and more of these like charges leads to collective effects because of **space charge** interactions, which become important or even dominant. Indeed, very intense beams are in effect non-neutral plasmas and exhibit a number of complex phenomena such as plasma waves and heating, making them both interesting and challenging. Hence, for practical applications, the **intensity frontier** can be as important as the more famous **energy frontier**.

Even in the case of high energy accelerators, where space charge effects are small after the initial low energy stages as discussed later, the beam usually starts in a space charge dominated regime. The collective effects at the early stages can cause a deterioration in the beam quality that is practically irreversible and affects the later, high energy stages.

The goal of this thesis is to study one particular complication that becomes important at high beam intensities, namely the appearance of a **halo** of particles around the main

beam. The existence of this halo manifestly deteriorates the beam quality, as well as introducing a number of secondary complications that hamper the operation and maintenance of accelerator facilities. Although the study focuses on the parameter regime relevant to the University of Maryland Electron Ring, the underlying phenomena are general. Hence, the results and conclusions will apply, mutatis mutandi, to a wider range of intense beam facilities.

1.2 Beam Halo and its importance in particle accelerators

Although there does not exist a commonly accepted, rigorous definition of halo for charged particle beams, halo is a common occurence in intense beams. One example is shown in Fig. 1.1, an experimental picture of the 23 mA beam at the University of Maryland Electron Ring (UMER).

The existence of halo is usually associated with a number of unwanted side effects:

1. Emittance growth, which decreases the beam quality, since both the size and the velocity spread of the beam increase.

2. Increased noise in the detectors, as halo particles participate in various interactions in an uncontrolled fashion.

3. Uncontrolled beam loss, which can damage sensitive parts of the transport channel as particles with high energy hit them.

4. Nuclear activation of the transport channel, if the highly energetic halo particles hit the beam pipe. This can hamper the maintenance of the facility as well as pose

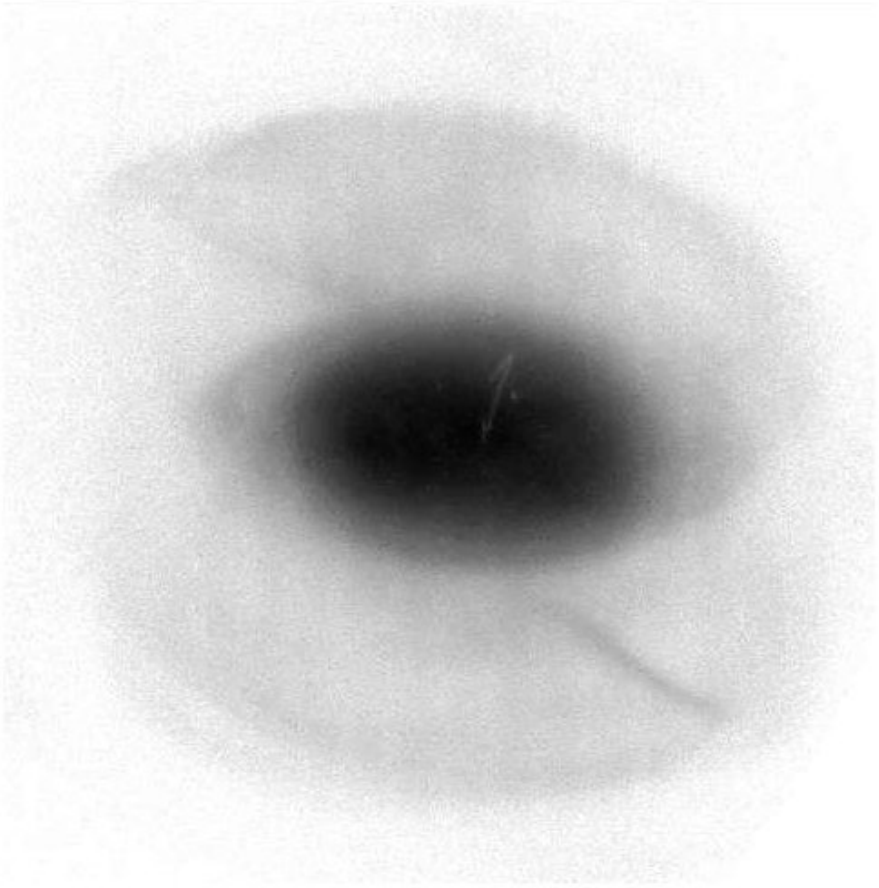

Figure 1.1: Experimental picture of a beam with halo in UMER.

potential health issues.

5. Emission of secondary electrons when particles hit the pipe wall, which creates and electron cloud around the beam and complicates the dynamics of the transport in the case of positively charged beams.

1.3 Beam halo in intense beams

Although beam halo is present in a wide range of accelerator facilities, it is a bigger concern in the case of intense beams. This is attributed to two main reasons:

1. A larger total number of particles means a larger absolute halo population

2. The appearance of halo is associated with collective effects, that are more important in intense beams.

The last effect has been known in the community [19] for some time. Indeed, Gluckstern [1] and Lagniel [20] were the first to use a **particle-core** model to describe the coupling mechanism between beam core oscillations and individual particles that can lead to halo creation. Building on that model, Wangler et al [21] concluded that there exists a maximum extent of the beam halo and this hypothesis was tested at the LEDA experiment in Los Alamos National Lab [22]. The LEDA experiment, as well as experiments at the spallation neutron source, were studied in the context of halo creation by Ryne et al using massively parallel simulations in [23]. Ikegami et al [24] discussed the effect of quadrupole focusing channels, again in the context of particle-core models. Qiang et al also discussed the effects of space charge in halo creation and emittance growth in [25].

The goal of this thesis is to build on those studies and in particular to take into account the issue of **self-consistency**. Indeed, although the collective force that couples the beam core to halo particles is a major factor in the creation of halo, the importance of other, concurrent collective effects cannot be overlooked. As will be discussed later, these can lead to a number of complications, such as the regeneration of halo.

A second goal is the study of beam halo due to non-ideal focusing fields, and in particular **skew quadrupoles**. For this purpose, we compare a modified particle-core model to self consistent particle-in-cell (PIC) simulations using the WARP code, as well as measurements at the University of Maryland Electron Ring.

1.4 Organization of the thesis

For this, we start in Chapter 2 by discussing the definition of beam halo and the current model for halo creation. In Chapter 3 we discuss the evolution of non-ideal beam distributions and the effect this has on beam halo. We also discuss the effect of mismatch on halo creation, the properties of the resulting halo as well as implications of these properties to the issue of halo removal or collimation. In Chapter 4 we discuss another type of mismatch, namely rotated quadrupoles, that complicate the symmetry properties of the system and also lead to beams with angular momentum, as well as complex halo structure. Finally, in Chapter 5 we summarize the results and present the conclusions of the thesis.

Chapter 2

The particle-core model of halo creation

As we mentioned in the Introduction, one of the fundamental goals of beam physics is to transport the maximum amount of current, keeping the transverse size and divergence of the beam minimal. One of the most important limiting factors in the transport of intense beams is the creation of a halo of particles around the main beam.

In this Chapter, we discuss the issue of halo definition and the theoretical basis of understanding halo creation in an intense charged particle beam.

2.1 Fundamental Quantities of Beam Dynamics

We start by introducing some of the basic quantities of beam physics and the assumptions that we make. Our first assumption is that the charged particles are well described by classical, relativistic dynamics [26]. Hence, we can fully describe a particle by its position $\boldsymbol{x} = (x, y, v)$ and velocity $\boldsymbol{v} = (v_x, v_y, v_z)$, in addition to its mass m and charge q.

In the case of a beam, the movement of the particles is highly directed in the longitudinal direction, which we define to be z. We can thus simplify our analysis by working in the so called paraxial approximation [27], in which case we have $v_{x,y} \ll v_z$ for the

transverse velocities and we can define:

$$x' = \frac{\mathrm{d}x}{\mathrm{d}z} = \frac{v_x}{v_z} \tag{2.1}$$

$$y' = \frac{\mathrm{d}y}{\mathrm{d}z} = \frac{v_y}{v_z} \tag{2.2}$$

The angles x' and y' are thus closely related to the velocities v_x and v_y and in the following the former will be used instead of the latter as phase space variables. In effect, we are changing the independent variable in our equations from time t to the longitudinal distance traveled z, a transformation very common in the context of beam dynamics [28].

In the case where all the particles have the same longitudinal velocity v_z, we can reduce the dimensionality of the problem from 6 to 4 dimensions. That is done by assuming that the beam is an infinitely long cylinder, and in the rest of the thesis we will treat the transverse phenomena as decoupled from the longitudinal physics, unless otherwise indicated. One further simplification that holds throughout the dissertation is that the beam is not being accelerated as it travels along the transport channel. Hence, the longitudinal velocity v_z is taken to be constant, unless otherwise indicated.

Assuming that the continuum limit holds well for the charge densities discussed [29], the most general description of the beam is contained in the Particle Distribution Function (PDF), which is a function of 6-dimensional phase space $f = f(x, v_x, y, v_y, z, v_z)$ and it is the particle number density at the point $\boldsymbol{x} = (x, v_x, y, v_y, z, v_z)$. Under the assumptions described above, we can simplify f to be a function in 4-dimensional phase space. Thus, we can define moments of the distribution, or average quantities, as in Eq. (2.3):

$$\langle g \rangle = \iiiint g f(x, x', y, y')\, dx\, dx'\, dy\, dy' \tag{2.3}$$

Two such quantities that are experimentally measurable and important are the **rms beam size** and the **rms beam divergence**, defined respectively in Eqs (2.4) and (2.5) for the x direction, while similar definitions hold for y.

$$x_{\text{rms}} = \sqrt{\langle x^2 \rangle} = \left(\int_{-\infty}^{\infty} x^2 f(x, x', y, y') \, d^2\boldsymbol{x} d^2\boldsymbol{x'} \right)^{1/2} \tag{2.4}$$

$$\theta_{x\text{rms}} = \sqrt{\langle x'^2 \rangle} = \left(\int_{-\infty}^{\infty} x'^2 f(x, x', y, y') \, d^2\boldsymbol{x} d^2\boldsymbol{x'} \right)^{1/2} \tag{2.5}$$

We should note that, in general, we do not expect the size or the divergence in x and y to be equal.

Measuring the beam size is a routine operation in accelerator facilities, although complications arise sometimes, especially when the diagnostic has to be non-destructive. The most widely used method is to place a screen in the beam pipe. When the charged particles hit the screen, photons are emitted and can be detected by a camera or other detection devices.

The beam divergence is also directly measurable, either by pinhole measurements, a method also used for measuring the divergence in laser beams, or by measuring the properties of the Optical Transition Radiation (OTR) emitted when the particle beam goes through a metallic foil [30]. The beam divergence is by definition related to the beam temperature T in the corresponding transverse direction, as shown in Eq. (2.6):

$$k_B T_{x,y} = \gamma m \left\langle v_{x,y} \right\rangle^2 = \gamma m v_z^2 \theta_{x,y}^2 \tag{2.6}$$

where k_B is Boltzmann's constant.

Another important characteristic beam quantity is the **generalized beam perveance**,

defined by:

$$K = 2\frac{I}{I_0}\frac{1}{\beta^3\gamma^3} \tag{2.7}$$

The characteristic current I_0 in (2.7) depends on the particle species and is defined in Eq. (2.8).

$$I_0 = \frac{4\pi\epsilon_0 mc^3}{q} \tag{2.8}$$

In the case of electrons or positrons, $I_0 \approx 17$ kA and for ions of mass number A and charge number Z, $I_0 \approx 31Z/A$ MA.

The importance of K becomes apparent when we write the expression for the space charge force acting on a single particle due to the particles that form the rest of the beam. For a uniform, circular, transverse beam distribution, we can show that this force is given by:

$$F(x) = \begin{cases} mv_z^2 \frac{K}{r^2} x & x \leq r_b \\ \\ mv_z^2 \frac{K}{x} & x > r_b \end{cases} \tag{2.9}$$

where x is the particle position and r_b is the beam radius. We note that in the case $x < r_b$, the space charge force is linear in x.

In Eq. (2.7) we see that K is a measure of the space charge forces within the beam. These forces scale with $(\beta\gamma)^{-3}$ and hence become less important at high energies, something we alluded to earlier. On the other hand, the external focusing force is usually magnetic for high energy machines and scales as γ^{-1} with increasing energy. Thus, with increasing values of γ, the space charge force decreases much faster than the external forces and for high energies the space charge force becomes neglibile.

The **emittance** of a beam is closely related to the beam temperature and the beam

entropy [31, 32, 33]. It is defined in (2.10) for the x direction and similar definitions hold for y.

$$\epsilon_x^2 = \langle x^2 \rangle \langle x'^2 \rangle - \langle x x' \rangle^2 \tag{2.10}$$

$$\epsilon_n = \beta\gamma\epsilon \tag{2.11}$$

It can be shown [27] that the emittance in Eq. (2.10) is conserved in the case of constant beam energy and forces linear in $\boldsymbol{x}$, whereas the **generalized emittance** of Eq. (2.11) is conserved even in the case of an accelerating beam. As was the case with size and divergence, we do not in general expect the emittances in x and y to be equal. The term $< xx' >$ that enters in Eq. (2.10) is called the cross-correlation term and is negative if the beam is contracting with increasing z and positive if the beam is expanding.

The beam emittance is widely used as a "figure of merit" for beam quality, since a low emittance requires both a small size and a small divergence. Indeed, the average beam brightness $\bar{B}$ is defined in Eq. (2.12).

$$\bar{B} = \frac{2I}{\pi^2 \epsilon_x \epsilon_y} \tag{2.12}$$

High brightness requires both high current I and low emittance in the x and y directions, thus giving us a quantitative measure to the concept of beam quality.

In Fig. 2.1, we see a beam with a flow that is close to laminar, or equivalently a low-emittance, high quality beam, while in Fig .2.2 we visualize a high emittance beam.

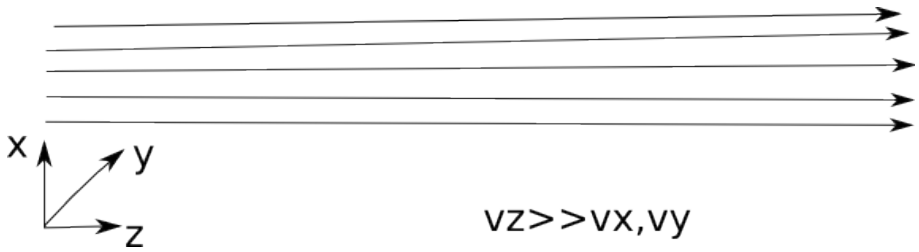

Figure 2.1: Laminar or low emittance beam

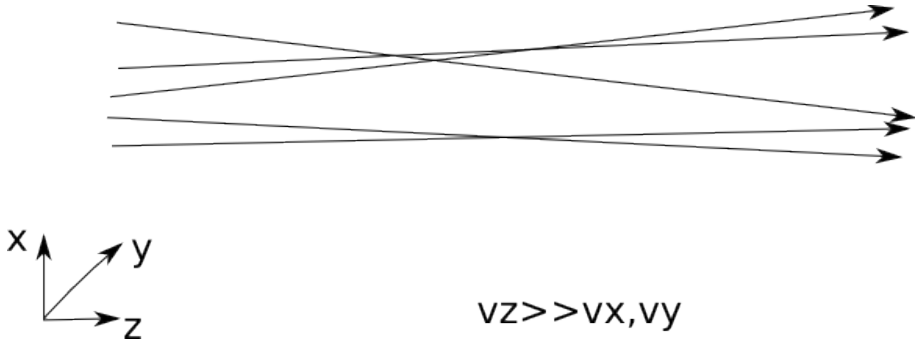

Figure 2.2: High emittance beam

2.2 Beam Envelope Equation

We now have all the quantities needed to write a moment equation that describes the evolution of the beam size transported in a round pipe. For this, we include the influence of the internal space charge force, which is linear in the case of uniform beams, and different types of external focusing, that can be electric or magnetic in nature.

2.2.1 Smooth focusing channel

Conceptually, the simplest focusing channel is the **smooth focusing channel**, where the external force applied to confine the beam is constant in z, azimuthally symmetric and a linear function of distance from the coinciding centers of the beam and the pipe. That is, the focusing force is given by:

$$F_q(x) = mv_z^2 k_0^2 x \tag{2.13}$$

where k_0 is a measure of the focusing strength and is called the betatron wavenumber.

As shown in [27] the single particle equation of motion is given in this case by (2.14).

$$\frac{\mathrm{d}^2 x}{\mathrm{d}z^2} + k_0^2 x = x \begin{cases} \frac{K}{r_b^2} & x \leq r_b \\ \frac{K}{x^2} & x > r_b \end{cases} \tag{2.14}$$

The evolution of the beam radius R can be obtained by taking moments over Eq. (2.14) and is given by Eq. (2.15).

$$\frac{\mathrm{d}^2 R}{\mathrm{d}z^2} + k_0^2 R - \frac{K}{R} - \frac{\epsilon^2}{R^3} = 0 \tag{2.15}$$

One realistic implementation of a smooth focusing channel is a long solenoid magnet, as is the case in the Long Solenoid Experiment (LSE) associated with UMER.

2.2.2 Alternating gradient focusing

A more common setup in particle accelerators is the **strong focusing** channel, also referred to as alternating gradient or FODO channel. In this case, the transport channel consists of magnetic or electric quadrupoles. Quadrupoles have the effect of focusing on one transverse direction while defocusing on the perpendicular transverse direction and by reversing their polarity, we can exchange the directions of focusing and defocusing. Hence, by placing magnets of alternating polarity along the transport channel, we can focus the beam on average. In this case, the beam no longer has an azimuthal symmetry, but instead the beam envelope is described by two quantities, its size in the x-direction,

X, and its size in the y-direction, Y. The envelope equations become now:

$$\frac{\mathrm{d}^2 X}{\mathrm{d}z^2} + \kappa(z)X - \frac{2K}{X+Y} - \frac{\epsilon_x^2}{X^3} = 0 \tag{2.16}$$

$$\frac{\mathrm{d}^2 Y}{\mathrm{d}z^2} - \kappa(z)Y - \frac{2K}{X+Y} - \frac{\epsilon_y^2}{Y^3} = 0 \tag{2.17}$$

where $\kappa(z)$ is given by:

$$\kappa(z) = \begin{cases} \kappa_0, & 0 < z < d \\ 0, & d < z < \frac{S}{2} - \frac{d}{2} \\ -\kappa_0, & \frac{S}{2} - \frac{d}{2} < z < \frac{S}{2} + \frac{d}{2} \\ 0, & \frac{S}{2} + \frac{d}{2} < z < S \end{cases} \tag{2.18}$$

where d is the length of the quadrupoles and S is the distance between two quadrupoles of the same polarity, or the periodicity of the FODO channel. The single particle equation of motion becomes in this case:

$$\frac{\mathrm{d}^2 x}{\mathrm{d}z^2} + \kappa(z)x = \begin{cases} \frac{2Kx}{X(X+Y)} & |x| \leq X \\ \frac{2Kx}{x^2 + |x|\sqrt{x^2+Y^2-X^2}} & |x| > X \end{cases} \tag{2.19}$$

and we have a similar equation for y. We note that although the envelope equations for X and Y are coupled, the single particle equations for x and y are not. Hence, we can focus on the motion of single particles along the x direction, without loss of generality.

The solutions admitted for the beam envelope in Eq. (2.15) are in general oscillatory. In the case of a uniform focusing channel (k = const), there can also exist a stationary solution, with $R'(z) = 0$ and $R(z) = R_m$ = const.. This case is commonly referred to as a matched beam, and the matched beam radius R_m is given by setting

$R'(z) = R''(z) = 0$ in Eq. (2.15), as shown in Eq. (2.20).

$$k_0^2 R_m - \frac{K}{R_m} - \frac{\epsilon^2}{R_m^3} = 0 \tag{2.20}$$

A plot of the beam envelope and a typical particle trajectory for the case of a matched beam is give in Fig. 2.3.

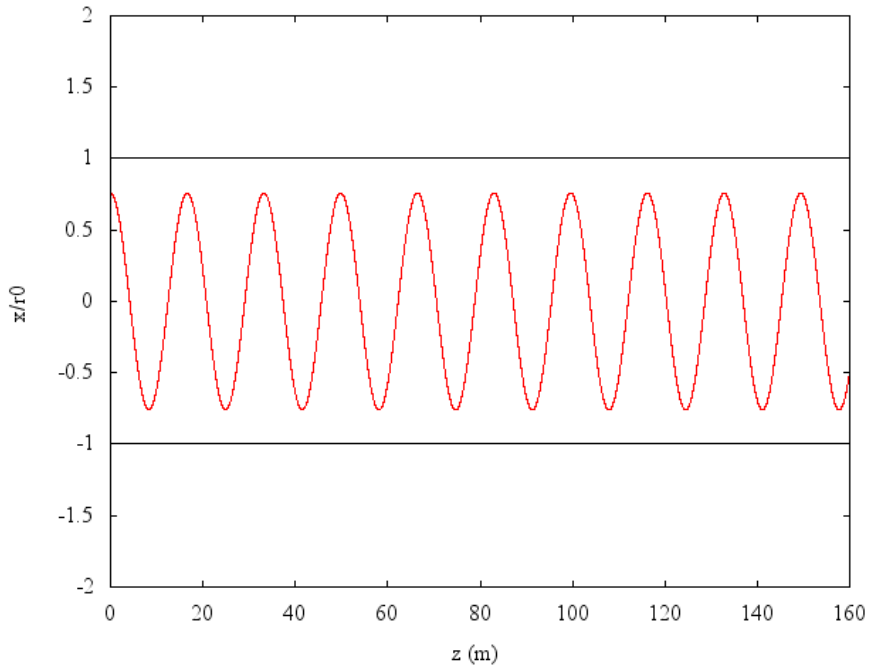

Figure 2.3: Plot of envelope (black) and single particle (red) for the case of a matched beam in a smooth focusing channel.

We see now that the beam envelope equation is essentially a balance between three forces, namely the external focusing force $F_f = k_0^2 R_m$, the internal space charge defocusing force $F_{sc} = \frac{K}{R_m}$ and the defocusing emittance force, which is closely related to pressure, $F_\epsilon = \frac{K}{R_m}$. The dimensionless ratio of F_f to F_{sc} is defined as the **intensity parameter** χ in Eq. (2.21) and is important as a measure of the effect of space charge for any given beam.

$$\chi = \frac{F_{sc}}{F_f} = 1 - \frac{F_\epsilon}{F_f} = \frac{K}{k_0^2 R_m^2} \tag{2.21}$$

The balance of forces requires that in order to have a matched beam $0 < \chi < 1$. Furthermore, in the case of $\chi < 0.5$ the emittance term is dominant, and hence we have an **emittance dominated** beam, while for $\chi > 0.5$ we have a **space charge dominated** beam.

In the more realistic case of a mismatched beam, we have $R'(z) \neq 0$ and there exists a periodic solution to the envelope equation. In Fig. 2.4, we show a plot of these envelope oscillations, along with an orbit of a single particle coupled to the envelope oscillations as described by Eqs. (2.15) and (2.14).

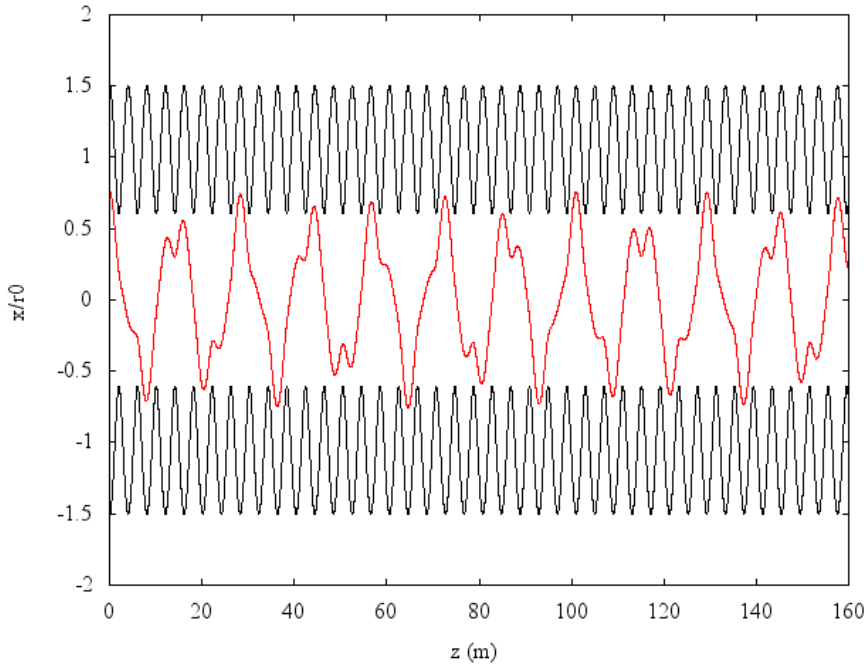

Figure 2.4: Plot of envelope (black) and single particle (red) for a breathing mismatch mode in a smooth focusing channel

In the context of alternating gradient focusing, a matched beam is defined as a beam where the envelope oscillations described by Eqs. (2.16) and (2.17) have the same periodicity S with the transport channel. That is, the beam envelope should appear the

same when strobed with a period S in the z direction, but it no longer has cylindrical symmetry.

In the case of a mismatch, there exist two (normal) modes of envelope oscillation, one where X and Y oscillate in phase (also known as a breathing mode) and one where they oscillate with a phase difference of π (the quadrupole mode). Of course this happens in addition to the oscillation due to the periodic focusing, and the result is a more complicated picture which will be discussed later.

2.3 Equilibrium Particle Distribution Functions

In the case of a uniform focusing channel, the transverse Hamiltonian function $H_\perp$ for a single relativistic particle is given by Eq. (2.22), as described in [34].

$$H = \sqrt{m^2c^4 + (c\boldsymbol{P} + e\boldsymbol{A})^2} \tag{2.22}$$

where $\boldsymbol{P}$ is the particle's canonical momentum and $\boldsymbol{A}$ is the vector potential.

For the reasons discussed earlier, intense beams are usually non-relativistic, in which case the transverse Hamiltonian function is given by (2.23).

$$H(\boldsymbol{x}, \boldsymbol{v}) = \frac{1}{2}m\boldsymbol{v}^2 + \frac{1}{2}k_0^2\boldsymbol{x}^2 + \psi(\boldsymbol{x}, t) \tag{2.23}$$

where k_0^2 is a measure of the external focusing force and the generalized potential $\psi(\boldsymbol{x}, t)$ corresponds to the self forces due to space charge [34]. It can be shown [34] that any function of the particle Hamiltonian is a stationary ($\frac{\partial f}{\partial t} = 0$) solution of the Vlasov equation in the case of constant k_0.

Three equilibrium particle distribution functions of particular importance are the Kapchinsky-Vladimirsky (KV) distribution, the waterbag (WB) distribution and thermal

equilibrium (TE) distribution, defined respectively by Eqs (2.24), (2.25) and (2.26).

$$f_{\text{KV}} = \delta\left(H(\boldsymbol{x},\boldsymbol{v}) - H_0\right) \tag{2.24}$$

$$f_{\text{WB}} = \Theta\left(H(\boldsymbol{x},\boldsymbol{v}) - H_0\right) \tag{2.25}$$

$$f_{\text{TE}} = C\exp\left(-\frac{H(\boldsymbol{x},\boldsymbol{v}) - H_0}{k_B T}\right) \tag{2.26}$$

where δ and Θ are the usual delta and step functions and H_0 is a characteristic energy value. The relatively simple mathematical properties of the KV and WB distributions make them amenable to analytical calculations, whereas the TE distribution is important since it is expected for thermodynamic reasons that the final state of the beam should be in this form [27].

In the case of a FODO channel, the only known equilibrium is the KV distribution. Significant work is being done towards the goal of constructing an equilibrium distribution function for the case of alternating focusing [35], although an analytical solution does not yet exist.

2.4 The University of Maryland Electron Ring (UMER)

The University of Maryland Electron Ring is a scaled electron experiment, used to study the effect of intense space charge in the transport of charged particle beams. Hence, the focus in UMER is to study the beam intensity limit, as opposed to the energy limit.

A schematic of the UMER ring is shown in Fig. 2.5

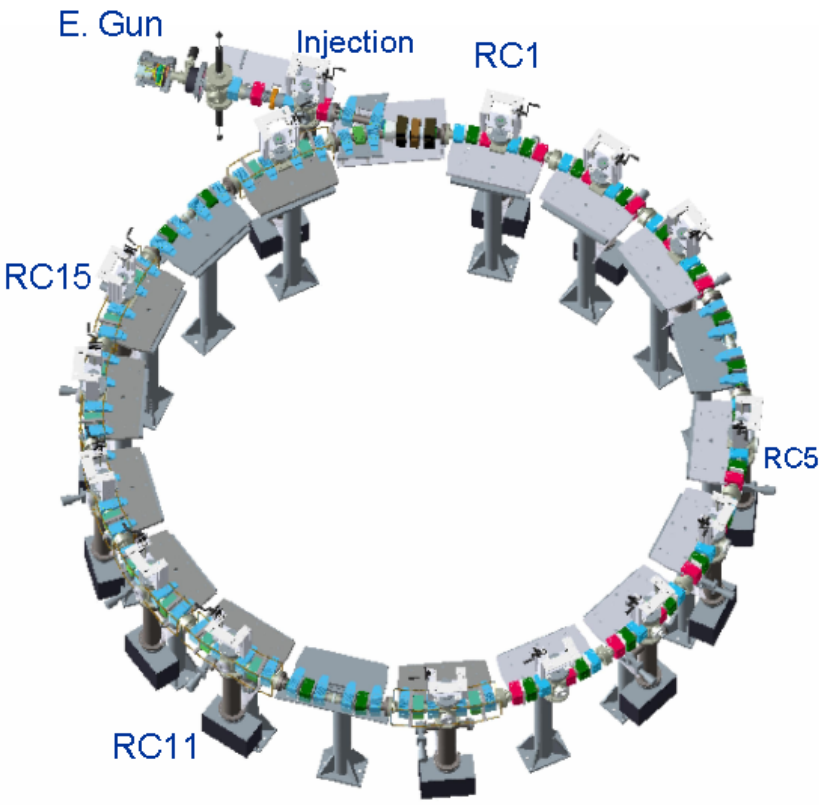

Figure 2.5: The University of Maryland Electron Ring. Courtesy of S. Bernal

Some important parameters of the UMER facility are given in Table 2.1.

Table 2.1: Parameters of UMER

Beam energy	10 keV	Typical pulse length	100 ns
Energy spread	10 eV	Circulation time	197 ns
Relativistic γ factor	1.02	Circumference	11.52 m
Relativistic β factor	0.2	Pipe diameter	15.875 mm
FODO period	0.32 m	Pulse rate	20-60 Hz

UMER is able to access a wide range of the parameter χ, by aperturing the beam and thus reducing the beam current. Important parameters for the various beams available

in UMER are given in Table 2.2

Table 2.2: Beams available in UMER, adapted from [36] and [37]

	a_0[a] (mm)	Current (mA)	Emittance (mm-mrad)	r_0[b] (cm)	χ	λ_p[c] (m)
Mask 1	0.125	0.7	7.6	1.5	0.27	2.06
Mask 2	0.875	7	25.5	3.19	0.6	1.39
Mask 3 [d]	5×0.375	5×5.6	86.6	8.7	0.32	1.89
Mask 4	1.5	23	39	4.89	0.84	1.17
Mask 5	2.85	78	86.6	8.7	0.90	1.13
Mask 6	3.2	104	97.3	9.92	0.92	1.12

[a] Aperture radius

[b] Average matched beam radius

[c] Plasma wavelength

[d] 5 apertures in a single mask

UMER is well suited to study the long term evolution of space charge phenomena, since it is a ring and thus the beam can recirculate, in contrast to linear accelerators (linacs).

The low energy of the beam allows real time interaction with the machine. On top of that, the various UMER beams are very reproducible, something that also facilitates operations and measurements, allowing us for example to integrate over many pulses without introducing variations to the beam.

We can separate the UMER transport channel into 3 different sections, namely:

1. The electron gun

2. The injection section

3. The ring FODO lattice

As discussed later, halo can arise due to phenomena in all three of these sections.

2.5 Mismatch oscillations as a source of parametric resonances

One of the mechanisms proposed to explain halo in intense particle beams is parametric resonance between core and single particle oscillations. Gluckstern [1] was the first author to suggest this mechanism, as he showed that space charge couples the oscillations of the beam core to particles oscillating outside the core. This way, energy is transfered from the core to the halo particles, driving them far from the core.

The analysis in [1] begins by assuming a "breathing" beam, that is a slightly mismatched beam in a continuous focusing channel that performs small amplitude oscillations. We can express these oscillations in r as $r(z) = r_0(1 - \epsilon \cos pz)$, where ϵ is a small number corresponding to the amplitude of the envelope oscillations and p is the constant wavenumber associated with these oscillations. We can now write, substituting in Eq. (2.14):

$$x'' + q^2 x = -\frac{K^2}{r_0^2} x \left(1 - \frac{r_0^2}{r^2}\right) \Theta\left(r - r_0\right) + \frac{2\epsilon K}{r_0^2} x \cos pz \Theta\left(r_0 - r\right) \tag{2.27}$$

where $q^2 = k_0^2 - K/r_0^2$ is the wavenumber of the single particle oscillations in the absence of envelope oscillations and $\Theta(u)$ is the step function. By making a change of variables

from x, z to $A = r_0\sqrt{w}$, Ψ:

$$\frac{x}{r_0} = A\sin\psi = r_0\sqrt{w}\sin\Psi \tag{2.28}$$

$$\psi = (2q - p)z + \gamma \tag{2.29}$$

and averaging over fast oscillations, we can show that there exists an integral of motion:

$$g(w)(1 - h(w))\epsilon\cos\Psi = f(w)\Delta - t(w) - C \tag{2.30}$$

where $\Delta = \frac{1}{(1+\sqrt{1+k_0^2/q^2})/2}$, C is an integration constant and f, g, h and t are functions of w only. We can now see that in the absence of envelope oscillations, $\epsilon = 0$ and hence the amplitude variable w is independent of the phase variable Ψ. For finite ϵ, we have a parametric plot of w vs Ψ as shown in Fig. 2.6: The plot of Fig. 2.6 corresponds to

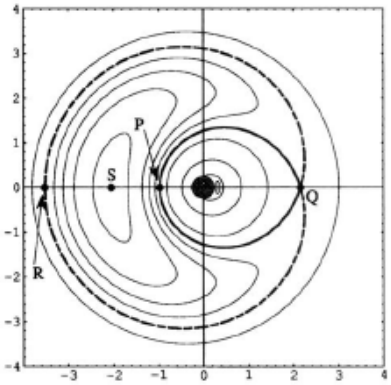

Figure 2.6: Polar plot of w vs Ψ from [1]

a period-2 map, since advancing z by $m/(2\pi p)$ or $2m/(2\pi q)$ results in the same phase Ψ. That is, two oscillations with wavenumber q correspond to one with wavenumber p. The topology of Fig. 2.6 consists of two regions and a separatrix as a boundary between them. The point Q is a period 1 unstable fixed point, while point S is a period 2, stable fixed point. All orbits originating between P and Q perform oscillations around the stable,

period 1 fixed point at the origin that are bounded by the separatrix. On the other hand, points outside the separatrix oscillated around the period 2 stable fixed point and can venture far from the beam core, to larger amplitudes w than the ones allowed inside of the separatrix. In other words, the points outside the separatrix are captured in a 2:1 resonance.

2.6 Chaotic orbits as a result of parametric resonance

The model in [1] has been numerically investigated by Wangler et al [21], where it is shown that these resonances can lead to chaotic orbits. In [21], the beam envelope equation is written in the normalized form:

$$\frac{\mathrm{d}^2 r}{\mathrm{d}\tau^2} + r - \frac{\eta^2}{r^3} - \frac{1-\eta^2}{r} = 0 \tag{2.31}$$

where $\tau = k_0 z$ and the parameter η is dimensionless and is related to the emittance and generalized perveance through $\eta = \frac{\epsilon}{k_0 R_0^2}$ and $1 - \eta^2 = K$ respectively. The matched solution corresponds to $r(\tau) = 1$, in which case $r'(\tau) = 0$. The equation of motion for a single particle becomes, under the same normalizations:

$$\frac{\mathrm{d}^2 x}{\mathrm{d}\tau^2} + x = \left(1-\eta^2\right) \times \begin{cases} x/r^2, & |x| \le r \\ 1/x, & |x| > r \end{cases} \tag{2.32}$$

It is obvious that in the case of $r(\tau) = 1$, Eq. (2.32) is not coupled to Eq. (2.31). Hence, since it is an autonomous second order ODE, it cannot exhibit chaos, as shown in the stroboscopic plot in Fig. On the other hand, if there is a mismatch, with a mismatch parameter $\mu = r(0) \neq 1$, Eq. (2.32) becomes coupled to Eq. (2.31) and the former is now

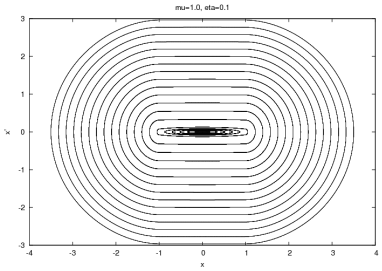

Figure 2.7: Stroboscopic plot of the phase space in the matched case

non-autonomous, since r depends on τ. Hence, it may admit chaotic solutions, and in fact it does, as shown in Fig. 2.8: In the left of Fig. 2.8, we have $\eta = 0.5$ and in the right

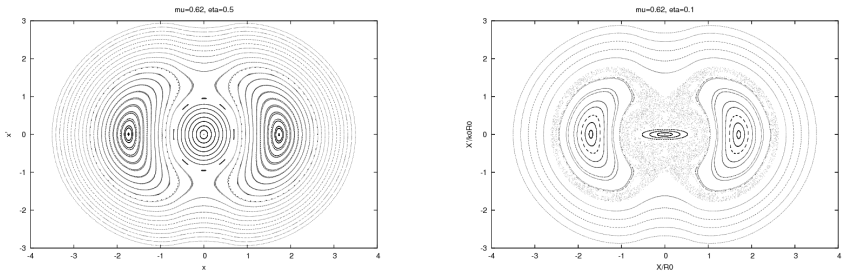

Figure 2.8: Stroboscopic plot of the phase space in the mismatched case, with $\mu = 0.62$

$\eta = 0.1$. Thus, as we decrease the parameter η from 1 (no space charge) towards 0, we see that the separatrix breaks and is eventually replaced by a chaotic region, as described in chapter 7 of the textbook [38].

Based on this model, Wangler et al where able to make empirical predictions about the extent of the halo. In particular, they found that x_max, the maximum extent of the halo, is related to μ, the mismatch parameter, through:

$$\frac{x_{\max}}{a} = A + B\,|\ln(\mu)| \tag{2.33}$$

where a is the beam radius corresponding to a matched solution and A, B are empirical parameters.

2.6.1 Periodic focusing transport channels

Ikegami [24] extended the particle-core model for halo creation to a periodic focusing channel. As we mentioned before, the picture is complicated in this case since there exist two oscillation modes, a breathing and a quadrupole one, in addition to the oscillation due to the periodicity of the focusing channel. Thus, in order to take a stroboscopic plot of the phase space, we need to adjust the parameters of the problem so the FODO period S and the envelope oscillation period, λ_b or λ_q for breathing and quadrupole modes respectively, are commensurate. Ikegami et al observed that the size of the chaotic region is bigger for the case of periodic focusing than in equivalent cases of continuous focusing, presumably due to the fact that the beam envelope is oscillating with a larger amplitude, as the beam is alternatively focused and defocused.

2.6.2 Experimental Measurements of Halo at LEDA

The prediction about the maximum extent of the halo stated in [21] was experimentally confirmed in Allen et al [22]. For this, they used linear alternating gradient accelerator at Los Alamos National Lab. By measuring the profile of the beam at the diagnostic points as a function of the mismatch parameter $\mu = r(0)$, they were able to confirm that the maximum extent of the halo follows the empirical law of Eq. (2.33):

In addition, Allen et al showed that the emittance growth resulting from halo creation was in agreement with the emittance growth predicted from thermodynamic arguments, as presented in [27].

2.7 Chapter Conclusion

In this Chapter we presented the basic concepts necessary to understand intense beam physics. Furthermore, we presented the theoretical background for halo creation, namely the particle-core model. As we saw, the collective effect of the beam core on individual particles can drive particles with appropriate oscillation phases to high amplitude oscillations, which manifest themselves as halo.

One of the important caveats of the particle-core model is the lack of self-consistency, as the halo particles do not affect the beam core. Additionally, the evolution of the core itself is simplified, as we assume a uniform beam with no internal degrees of freedom. The rest of this thesis will address these shortcomings of the particle core model, and test the predictions of the model against more accurate, self consistent simulations.

Chapter 3

Halo Creation in a Smooth Focusing Channel

3.1 Introduction

In this Chapter we discuss the effect of an initial mismatch in the creation and propagation of beam halo. The theoretical basis for understanding halo creation in this case was presented in Chapter 2, were we discussed the particle-core model. As we mentioned there, this model is not self consistent in two important ways:

1. The halo population does not couple to the main core population.

2. The model used to propagate the beam core assumes that the core keeps a constant emittance and a uniform charge distribution.

In order to investigate how well these assumptions hold, we compare the theoretical model with more accurate, self-consistent simulations. For this we use the WARP code which addresses the issues mentioned and also allows us to track the halo particles in the full 4-dimensional phase space.

WARP also allows us to investigate the effect of halo removal, as well as the properties of the halo population in different phase space projections.

Table 3.1: Beam Parameters used in WARP simulations

Current	$23\,mA$	Betatron wavenumber	$\sqrt{10}\,m^{-1}$
Emittance	$48\,mm-mrad$	Beam radius	$6.31\,mm$
Beam Energy	$10\,keV$	χ	0.82
Gen. Perveance	3.3×10^{-4}	k/k_0	0.42

3.2 Simulation Setup

In order to compare with the particle-core model, we will assume a uniform focusing channel, as the one used in Chapter 2. Furthermore, we assume an intense, non-relativistic electron beam, with parameters given in Table 3.2, where the generalized perveance K, the intensity parameter χ and the depressed betatron wavenumber k/k_0 are defined as follows:

$$K = \frac{eI}{2\pi\epsilon_0 m v^3} \tag{3.1}$$

$$\chi = \frac{K}{k^2 a^2} \tag{3.2}$$

$$\frac{k}{k_0} = \sqrt{1-\chi} \tag{3.3}$$

Since $\chi > 0.5$, the beam under study is a space charge dominated beam, corresponding to parameters close to the ones studied experimentally at the University of Maryland Electron Ring (UMER).

The plasma wavelength λ_p associated with these parameters is $\lambda_p = \lambda_0/\sqrt{2\chi}$ where λ_0 is the betatron wavelength. In our case $\lambda_0 \approx 1.99$ m and $\lambda_p \approx 1.55$ m and hence 100 m, the typical distance in the following simulations, correspond to approximately $65\lambda_p$.

This distance is sufficient for damping of mismatch oscillations to occur, as we see in the simulations.

We initialize the beam with four different initial distributions, namely a semi-gaussian (SG), a waterbag (WB) a Kapchinsky-Vladimirsky (KV) and a thermal equilibrium (TE) [27]. As discussed before, the KV, WB and TE distributions are equilibrium solutions of the Vlasov equation, but the SG distribution is not.

3.3 Definition of Beam Halo

Various exact definitions of beam halo have been proposed, based on the non-monotonicity of the particle transverse density [1], the kurtosis of the beam distribution [39] or the oscillation frequencies of the halo particles [40]. In addition, less rigorous definitions such as "uncontrolled beam losses" and "anything undesirable" are popular among practitioners. Indeed, in the day-to-day operation of accelerator facilities, any part of the beam that deviates from the ideal and has sufficiently low intensity is labeled as halo.

For our purposes, a particle will be considered to be in the halo if it ventures sufficiently far from the beam center compared to the beam size. That is, a particle outside the ellipse drawn in Fig. 3.1 will be considered as a halo particle.

Quantitatively, the condition described in Fig. 3.1 is given in Eq. (3.4):

$$\frac{x_i^2}{4X_{\text{rms}}^2} + \frac{y_i^2}{4Y_{\text{rms}}^2} > \rho \tag{3.4}$$

where (x_i, y_i) is the particle position in x and y respectively, $(X_{\text{rms}}, Y_{\text{rms}})$ the rms beam size in the x and y directions and ρ and adjustable parameter. By changing ρ we can

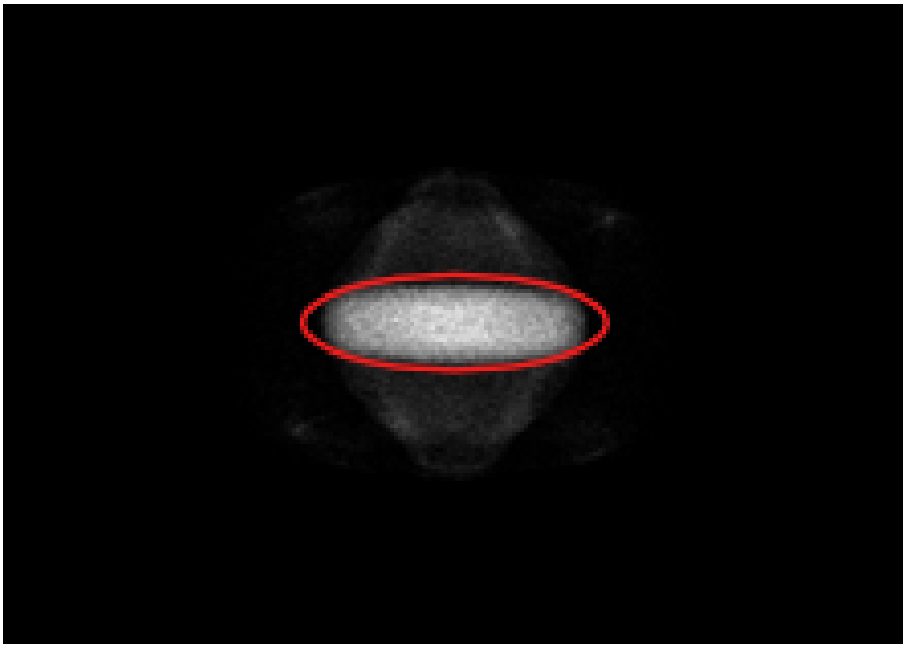

Figure 3.1: A typical beam exhibiting halo in WARP simulations. Any particles outside the red ellipse are defined as halo.

distinguish various different halo populations.

We should note that the beam edge becomes more abrupt for space charge dominated beams. Indeed, as we see in Fig. 3.2, the high space charge beam has a sharper edge, since the Debye length associated with it is smaller[1]. The sharper edge in the case of high space charge means that in principle we should expect fewer particles outside the beam core compared to the low space charge case. Thus, for high space charge, almost all the particles outside the beam core can be attributed to halo.

3.3.1 Determining the appropriate halo radius

In order to check if the particles labeled as halo according to our definition enter the halo one or more times, we can calculate the percentage of the time each particle has

[1]For a discussion on the connection between neutral and non-neutral plasmas see Appendix A

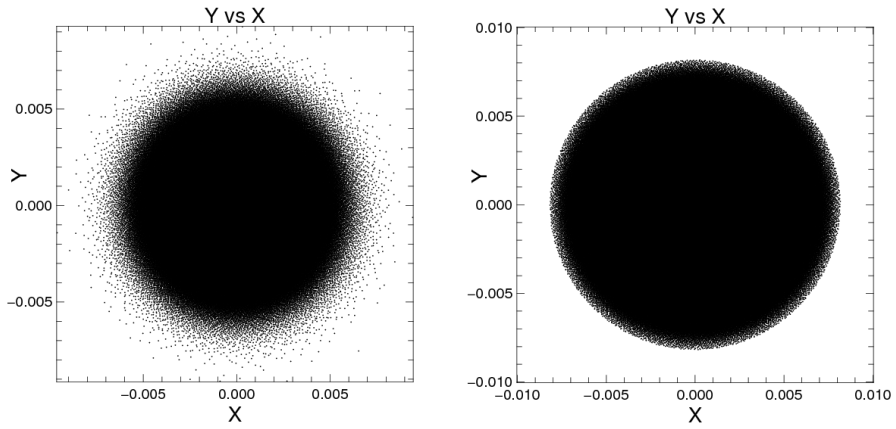

(a) TE distribution for low space charge (b) TE distribution for high space charge

Figure 3.2: Projection in $x - y$ for a TE distribution for low (23 μA) and high (23 mA) space charge. Note the more diffuse edge of the low space charge beam

spent in the halo. In Fig. 3.3 we plot the distribution of these percentages, for different values of the ρ parameter defined in Eq 3.4.

One important feature of Fig. 3.3 that the maximum of the distribution decreases with increasing values of ρ. This is to be expected, since the further away we put the halo boundary, the longer it takes the particles to reach it.

Another feature that justifies our use of this halo definition is that a very small number of particles spends a short time in the halo. Thus, we have a strong indication that most of the particles labeled as halo by our algorithm do indeed re-enter the halo and are not just singular outliers. In the following, we use the criterion of Eq. (3.4) with ρ =1.9, but save the halo particles for a range of halo radii.

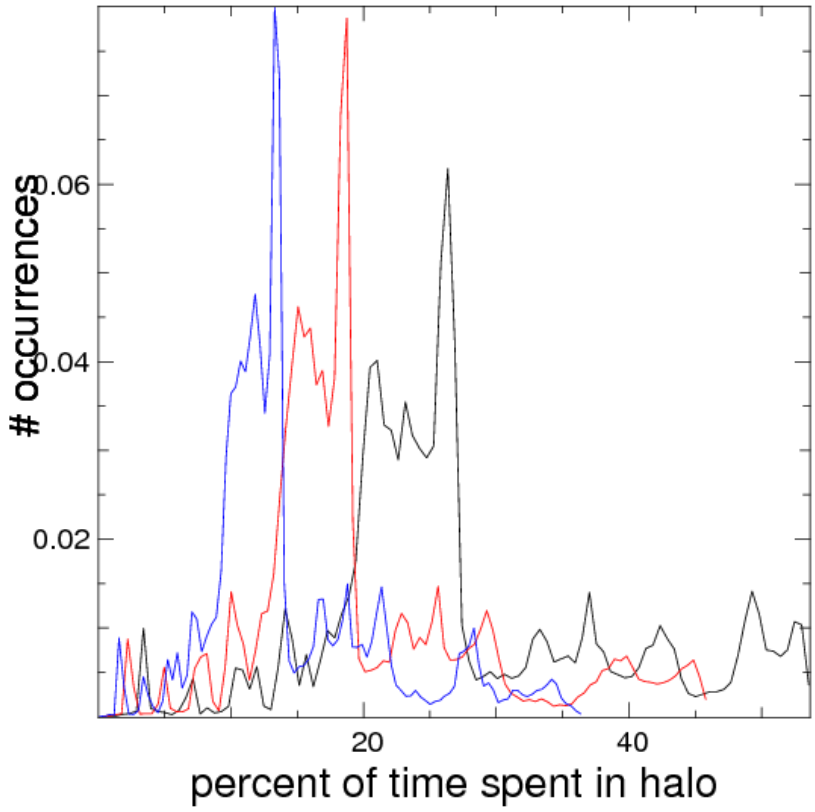

Figure 3.3: Histogram of times spent in the halo according to definition of Eq. 3.4 for ρ =1.5 (black), 1.7 (red) and 1.9 (blue). Note that only a small number of particles spend a small fraction of their time in the halo for all cases, and most of the particles re-enter the halo.

3.4 Convergence of PIC simulations

A common problem in the case of long numerical simulations is the issue of error propagation. As is well known, the numerical error in the rms moments when we approximate the continuous particle distribution function with N particles is of order $O(\frac{1}{\sqrt{N}})$ [41]. Hence quantities that depend on the beam moments, such as the total space charge force acting on particles, will have an error of the same order.

Additionally, in the case of halo studies, the halo population is in general much smaller than the main beam population. This forces us to use a high total number of particles, in order to ensure that the statistics in the halo, as well as the core, are satisfactory.

The results presented in the rest of this thesis have been thoroughly tested and shown to have the appropriate scalings with increasing number of particles. In particular, for most of the cases, it was found that 10^6 particles were sufficient and the results were convergent and agreed with the case of $N = 4 \times 10^6$. This number is roughly an order of magnitude bigger than the 10^5 required for convergence, for the same simulation length, when we are only interested in second order moments such as size and emittance.

The numerical errors relevant to our simulations can be broadly classified into two categories:

1. Errors due to the finite accuracy of the arithmetic operations performed by the computer.

2. Errors due to the finite accuracy of the numerical methods used to calculate the electromagnetic fields and propagate the particles.

For the numerical parameters used in this thesis, the first class of errors is much

smaller than the second and can be addressed by increasing the accuracy of the number type used. For all the simulations presented, we used **double precision** arithmetics, which are sufficiently accurate for the length of simulations performed.

In the case of the WARP PIC code, we used a leap-frog method for the numerical integration of the differential equations describing the particle trajectories. This method is known to be symplectic [42], that is it preserves the symplectic structure of the underlying physical system, assuming the latter is Hamiltonian.

This has important implications for the numerical stability of the simulations, as symplectic integrators solve a Hamiltonian system to machine precision. The errors in this case are due to the finite order of the method, since the integrator solves to machine a Hamiltonian system that deviates from the desired one.

The leap-from integrator used is a second order method with regards to the step size, that is the error per step is of the order $O((dz)^3)$. The most important condition in choosing a step size is to have enough steps to resolve the relevant length scales. In the case of a mismatched beam in a smooth focusing channel, the relevant length scale is the plasma wavelength, which is of the order of 1.55 m, much larger than the step used which is dz =4 mm.

In order to have good spatial resolution, we need to resolve scales less than a Debye length, particularly within the core. In the following simulations, the scale for dx and dy was 0.195 mm, roughly 4 times smaller than the transverse Debye length which was 0.9 mm. On the other hand, we need to make sure that enough macroparticles are within a cell in order to avoid statistical errors. Within the beam core, we have around 20 macroparticles per cell, whereas in the halo region the occupancy is much lower. This

could lead to problems due to self-fields in the halo region, but the dominant fields there are the external focusing and the electric field from the bulk of the beam. That is, the field from a single particle is much smaller than the long range fields, and hence errors in it do not severely affect the convergence properties of the simulation.

Another issue that can affect the accuracy of PIC simulations is the finite number of macroparticles used. As discussed before, in most of our PIC simulations we used 10^6 macroparticles to simulate the behavior of a real system comprising of 10^9. Some numerical phenomena associated with a small number of macroparticles in PIC codes are **numerical collisions** [43] and **averaging errors**.

In order to ensure that the phenomena observed in our simulations were real, we scaled up the number of particles by a factor of 4. If numerical collisions or other numerical artifacts associated with the number of macroparticles were present, the results should differ in the measurable quantities, such as emittance or, specific to our case, the number of particles in the beam halo. This was not observed, and indeed both these metrics were very close for runs with 10^6 and 4×10^6 particles. In particular, for a sample run the first case exhibited a final emittance of 49.1582541 mm-mrad, while the value from the second run was 49.0127378 mm-mrad. This corresponds to a fractional error of $\frac{|49.0127378-49.1582541|}{49.0127378} \simeq 0.3\%$. On the other hand, the error expected in average quantities such as the emittance is of the order $\frac{1}{\sqrt{N}} \simeq 0.1\%$, that is both errors are of the same order of magnitude.

The distribution of halo particles in the two cases is shown in Fig. 3.4, where the halo particles are ploted with red, and the core particles with black. The percentage of particles in the halo is 0.6872% for the case with $N = 10^6$ and 0.682275% for the

$N = 4 \times 10^6$ case, giving a fractional error of $\sim 0.7\%$, again in the same order of magnitude as the $\frac{1}{\sqrt{N}}$ limit.

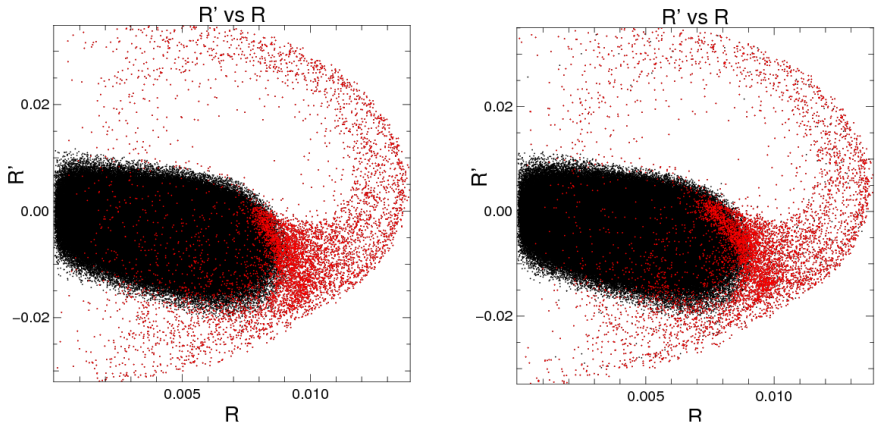

(a) 10^6 particle simulation (b) 4×10^6 particle simulation

Figure 3.4: Comparison of halo creation under identical conditions for $N = 10^6$ (left) and $N = 4 \times 10^6$ (right) macroparticles. Only 10^6 particles are plotted for the second case. The percentage of particles in the halo is the same for both cases, within the averaging error.

As discussed in Chapter 2, we expect a number of particle trajectories during the halo creation process to be chaotic, at least intermittently [44]. This can complicate the comparison of our numerical model to a physical system, since by definition chaotic systems exhibit **sensitive dependence** on initial conditions. This problem is of course not unique to simulations of particle beams, but is relevant for all chaotic systems. Discussions in the literature [38, 45] suggest that the property of **shadowing** can alleviate that problem. The shadowing property states that even though the true trajectory of a particle diverges from the simulated trajectory, there exists a real particle, different than the original one, with a trajectory close to the simulated trajectory. Thus, even though tracking

single particles is subject to the problem of sensitivity to initial conditions, tracking global properties, such as the phase space structure, is more reliable.

The numerical parameters used in our simulations are given in Table 3.2.

Table 3.2: Input parameters for the WARP code

Number of particles	10^6	Timestep dt	6.84×10^{-11} s
Grid size $n_x \times n_y$	512×512	Step size dz	4 mm
Particle weight [a]	2362	Number of steps	25000

[a] number of real particles corresponing to one macroparticle

3.5 Initial Distribution Effects

3.5.1 Evolution of the beam distribution

In real accelerators, the Particle Distribution Function f is neither a simple function of the phase space variables nor an equilibrium solution of the Vlasov equation (A.4). Hence, the PDF evolves in time, instead of remaining at an equilibrium state and can exhibit a very complicated structure [46, 47].

Indeed, it has been known since the 1970s that in the case of intense beams, internal oscillatory modes can arise in the case of mismatch. Gluckstern [46] was the first to study the stability of these modes, using a Kapchinsky-Vladimirsky model for the beam distribution. The stability analysis was extended to a more physical warm fluid model of the beam by Lund and Davidson in [47], where they recovered some, but not all, of the modes predicted by Gluckstern.

Recent work by Lund et al [48, 49, 50, 50] has extended the stability analysis further, predicting instabilities that can lead to rapid halo creation in the case of intense focusing of the beam. In the rest of this Chapter, we take care to avoid these rapid instabilities, by applying a weaker focusing force than the one discussed by Lund.

3.5.2 Beam distributions arising from the electron gun

In the case of a thermionic gun, the electrons being emitted from a heated cathode, are expected in general to have a uniform distribution in configuration space, assuming a uniform cathode surface, and a gaussian distribution in the velocities of the particles, with variance related to the cathode temperature.

Such a distribution is known as a semi-gaussian (SG) and, as discussed, is not in equilibrium but has been shown to evolve and to exhibit transverse space charge waves. The functional form of the SG distribution is given in Eq. (3.5)

$$f_{\mathrm{SG}} = n_0 \exp\left(-\frac{m\boldsymbol{v}^2}{k_B T_\perp}\right) \tag{3.5}$$

where n_0 is the constant, transverse number density and $T_\perp$ the transverse electron temperature.

Additionally, in the case of the UMER gun, we have a grid biased at a voltage value 30-45 V, in order to control the beam pulse. This has been shown [51, 36] to lead to a hollow velocity distribution. Furthermore, the geometry of the gun can lead to a significant halo population, as discussed in [3]. The former case can complicate the phase space dynamics, but does not lead to halo by itself, whereas the latter case has been corrected by improved alignment of the cathode. Hence, in the following we will focus

on the SG distribution, since it is the more general case.

3.5.3 Comparison of different initial distributions

In Fig. 3.5, we show the evolution of the emittance for four different initial distributions, the KV, WB and TE which are equilibria and the SG which is not. We note that

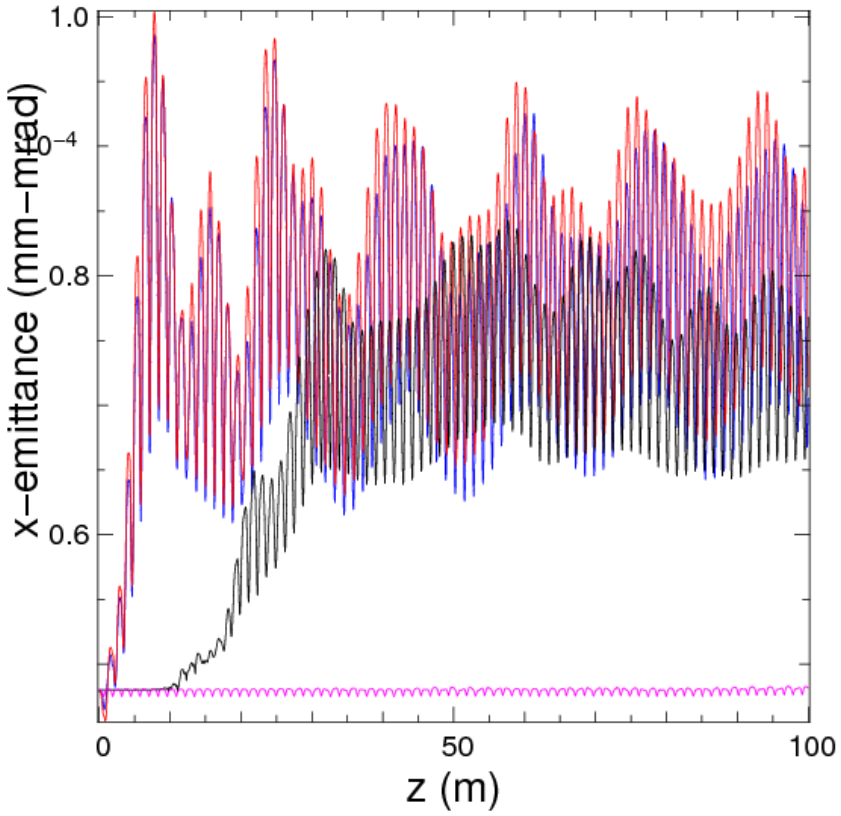

Figure 3.5: Emittance evolution for 4 different initial distributions that are mismatched. KV:black, SG: red, TE:blue, WB:magenta

the TE and SG distributions exhibit very similar behaviour, whereas the KV has initially lower emittance but eventually ends up in the same emittance value as the former two. The WB distribution does not exhibit any emittance growth.

Furtermore, in Fig. 3.6 we show the evolution of the total number of halo particles with z, the distance travelled. As was the case with emittance, the TE and SG distributions

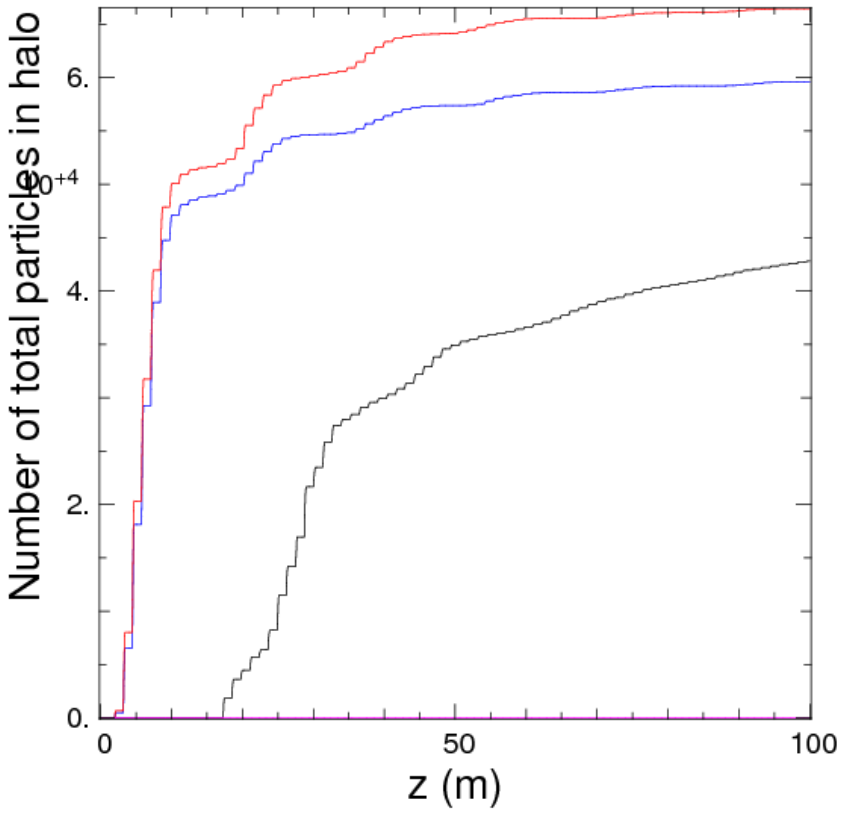

Figure 3.6: Evolution of the total number of halo particles for 4 different initial distributions that are mismatched. KV:black, SG:red, TE:blue,WB: magenta

follow each other closely, whereas the KV shows a slower build-up of the halo. Again, the WB distribution shows no halo creation.

In order to understand why the KV and particularly the WB distributions show a different behavior, we need to take into account their singular character. As we saw in the definition of those distributions in Eqs. (2.24) and (2.25), their projections in config-

uration space have a sharp boundary. That is, for these two distributions, there do not exist particles outside the beam core initially, which means that no particles can satisfy the 2:1 resonance condition, as discussed in Chapter 2. Hence, because of this unphysical constraint, the creation of halo is suppressed in these two cases.

In the case of the KV distribution, the particle population is inverted [52] in the sense that all the particles have the same energy. This causes the KV to be unstable, and thus after a few oscillations of the beam core the instabilities grow and particles can escape from the sharp boundary of the beam and eventually create the halo. On the other hand, the WB distribution does not exhibit instabilities, at least for this value of perturbation and in the length scale under study, and the particles are contained within the beam core.

Another important point is that the total emittance of the beam converges for the three cases where halo is present, whereas the number of halo particles does not. This is attributed to the fact that the free energy associated with the introduction of the perturbation is the same for all cases, and is much higher than the internal free energy differences of the various distributions. Thus, as discussed in Ref. [27], the available energy for thermalization that leads to emittance growth is roughly the same, as long as the appropriate mechanism for halo creation exists.

Furthermore, we can intuitively see that the particles in the halo are screened from the electric field fluctuations within the beam core and are only affected by the total field. On the other hand, particles within the beam core are affected by these fluctuations, which can change the phase and frequency of their oscillatory trajectories. Thus, we expect that different internal fields will lead to different particles satisfying the 2:1 resonance condition with the core oscillations, and thus create the halo.

3.5.4 Clump tracking

We can visualize the evolution of localized regions of phase space by tracking small clumps of particles, a standard tracer method in simulations [53]. Hence, we seed particle clumps with small size and velocity spread, at different location within the 4-dimensional phase space.

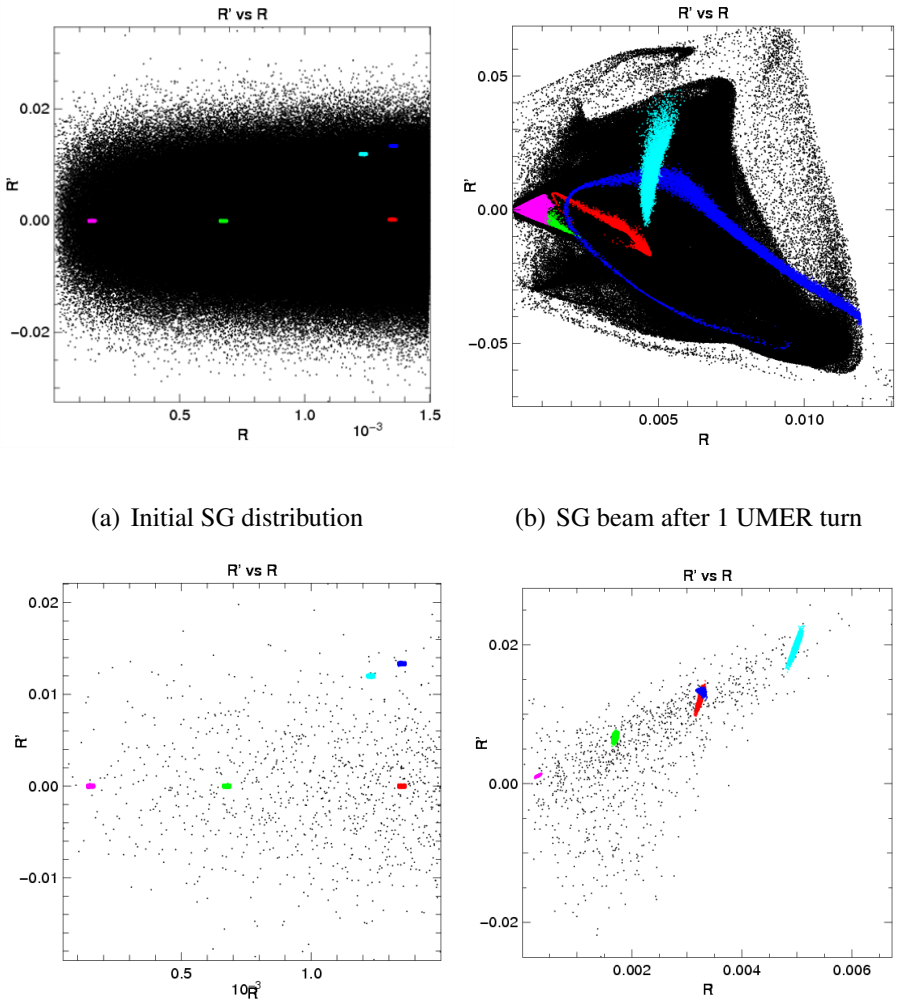

(a) Initial SG distribution

(b) SG beam after 1 UMER turn

(c) Initial 0 current beam

(d) 0 current beam after 1 UMER turn

Figure 3.7: Evolution of localized particle clamps in phase space for a SG and a 0 current beam

As shown in Fig. 3.7, the evolution of localized tracers in phase space varies greatly

in the different cases. Moreover, comparing Fig. 3.7(d) that corresponds to a zero space charge beam with Fig. 3.7(b) that corresponds to an intense beam, we see that the clumps stay localized in the first case, but not in the second.

We can quantify the evolution of the clumps by using the clump emittance as a measure of the area in phase space. In this case, the clump emittances in the case of the 0 current beam show roughly linear growth, while some of the clumps in the SG beam exhibit exponential growth in emittance, as shown in Fig. 3.8

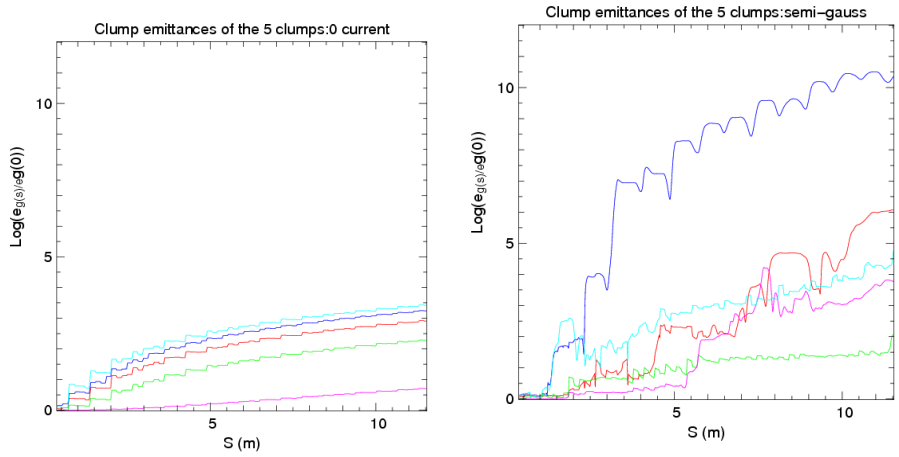

(a) 0 current clump emittances (b) SG clump emittances

Figure 3.8: Evolution of clump emittance for the 0 current and the SG case. Color coding corresponds to Fig. 3.7. Note the logarithmic scale.

This is an example of the complexity exhibited by intense beams, since this spreading of localized regions in phase space indicates that the properties of individual particles, such as their oscillation frequency and phase, cannot be assumed to remain constant, and indeed vary greatly. In Chapter 2 we discussed the dependence of halo creation on the resonance properties of individual particles, which were then assumed to be constant.

3.6 Phase space distribution of halo population

In this section, we discuss the properties of the phase space distribution of the halo, when the initial mismatch leads to a breathing oscillation mode of the beam envelope.

In particular, we see that in the cases where a halo develops, the halo particles occupy a peanut-shaped region of $r - r'$ space, indicating that the dynamics of halo creation are indeed described by the parametric resonance process outlined in [1, 21].

Since the beam distributions used in the simulations have cylindrical symmetry, plots is the $r - r'$ projections of phase space are better suited to capture the underlying symmetries, whereas projections in x or y can be misleading.

In Figs. 3.9, 3.10 and 3.11, we show the $r - r'$ phase spaces for 3 different cases of the thermal equilibrium distribution, a matched case, a case with 20% mismatch that shows little halo corresponding to 0.687% of the total particle number and a case with 50% mismatch that shows a more extensive halo, corresponding to 5.963% of the total particle population.

3.6.1 Spatial distribution of the halo particles

As we noted in the preceding section, the particles that constitute the halo population are distributed almost uniformly in $x - y$ space. That is, at each instance only a portion of the total halo population is outside of the beam edge, while the remainder appear within the beam core in the transverse $x - y$ projection. This has important implications for halo removal, to be discussed later.

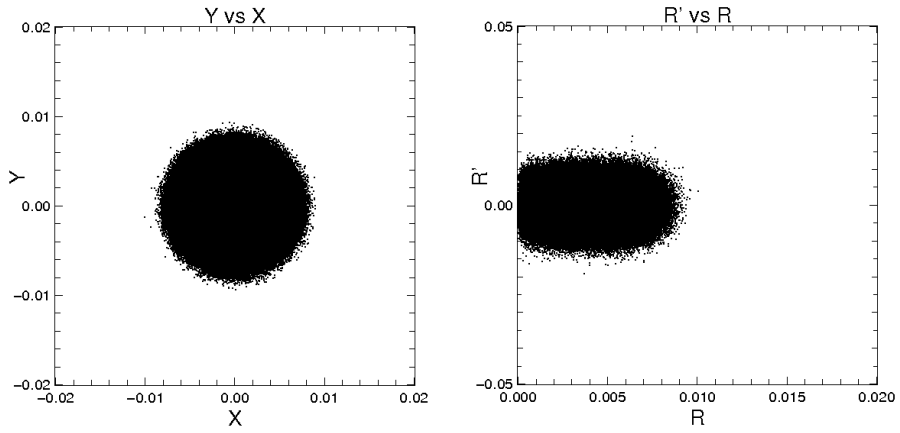

(a) $x - y$ space (b) $r - r'$ space

Figure 3.9: Matched case, no halo observed in $x - y$ or $r - r'$

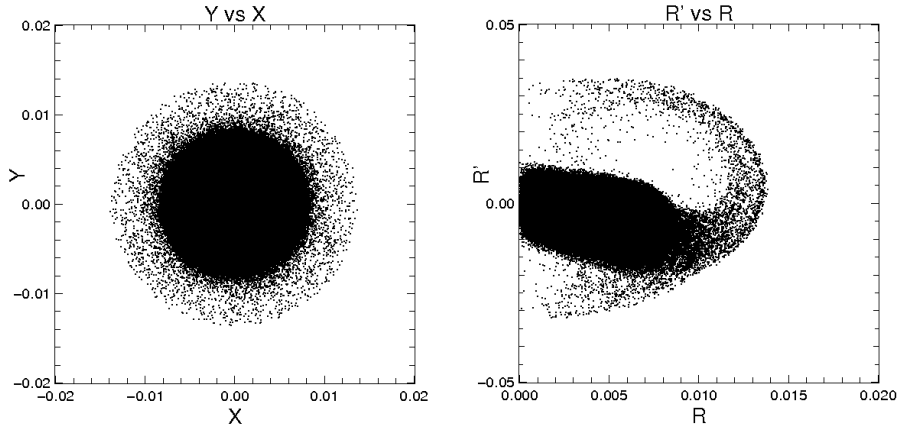

(a) $x - y$ space (b) $r - r'$ space

Figure 3.10: 20% mismatch case, halo is 0.7% of total particles and is observed in both projections

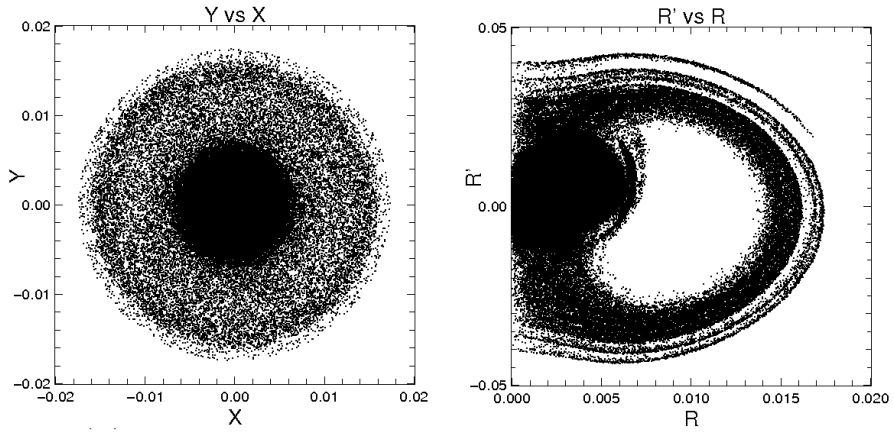

(a) $x - y$ space (b) $r - r'$ space

Figure 3.11: 50% mismatch case, halo is 5.9% of total particles and is observed in both projections

3.6.2 Velocity distribution of the halo particles

The velocity space projection of the beam core (black) and the beam halo (red) particles is shown if Fig. 3.12.

We can furthermore apply a similar criterion for the definition of halo in velocity space as the one in configuration space, as given in Eq. (3.6).

$$\frac{x_i'^2}{4\theta_x^2} + \frac{y_i'^2}{4\theta_y^2} > \rho \tag{3.6}$$

where x_i', y_i' are the particle velocities in x and y and θ_x, θ_y the rms beam divergence.

The **total halo** population as defined by Eq. (3.6) is found to be practically identical to the one defined according to the criterion of Eq. (3.4), as shown in Fig. 3.13

We should note that the evolution of the total halo population is not identical for the

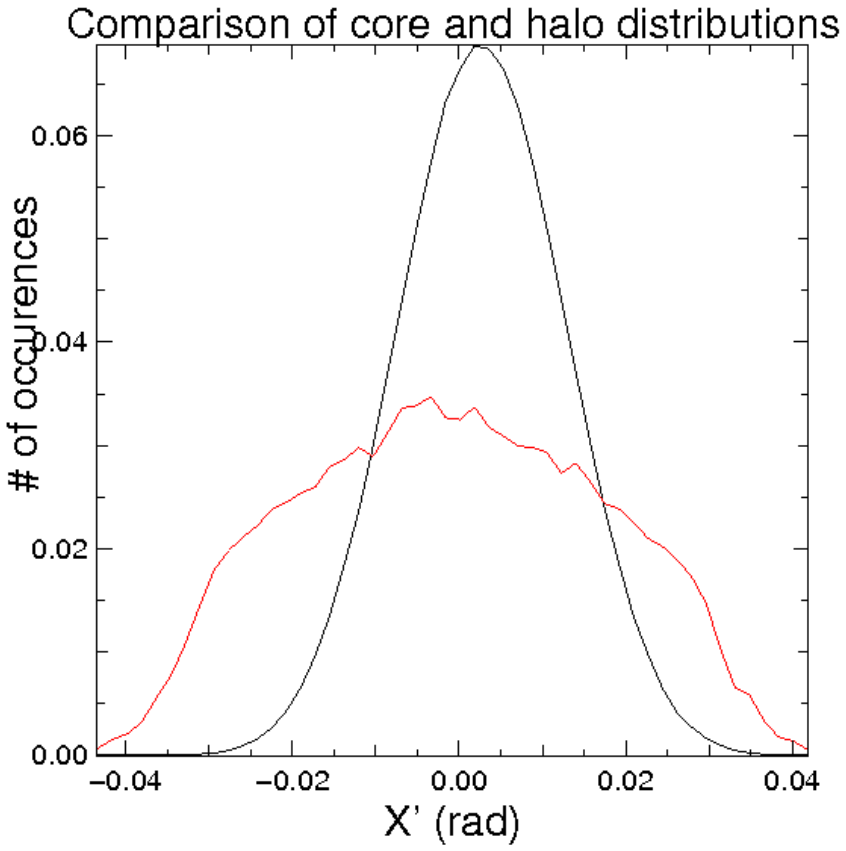

Figure 3.12: Velocity space distribution of core (black) and halo (red) particles. Note that the halo has a bigger rms divergence

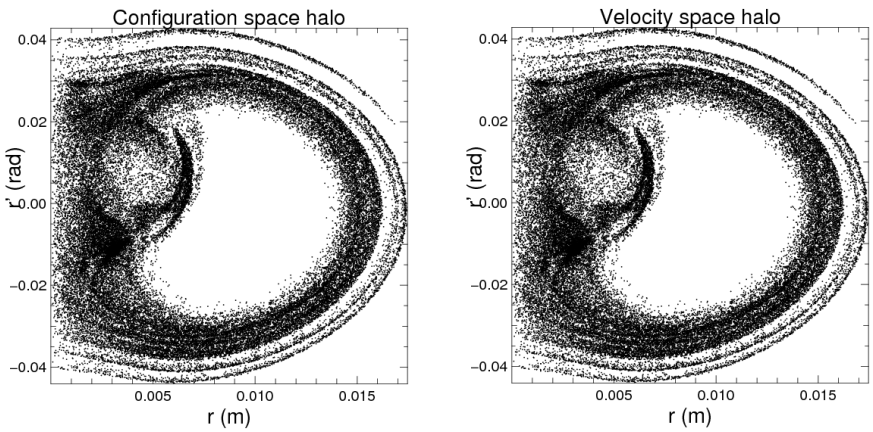

(a) Configuration space halo population (b) Velocity space halo population

Figure 3.13: Comparison of the total halo population according to the criteria in Eqs. (3.4) and (3.6). Note that the populations derived by the two separate criteria are identical.

2 criteria, but eventually leads to the same number, as shown in Fig. 3.14

Associating a bigger rms divergence, as well as a rms size, to the halo population has important implications for diagnostics, such as Optical Transition Radiation [54]. In Ref. [54] it was observed that for certain complex beams, the best fit with the experimental data was obtained under the assumption that the beam consisted of two separate populations in $x-y$, with two different rms sizes, and two separate populations in $x'-y'$, with two distinct rms divergence values.

This observation is supported by the simulations presented here, as the halo population is associated with rms size and divergence higher than the ones corresponding to the beam core.

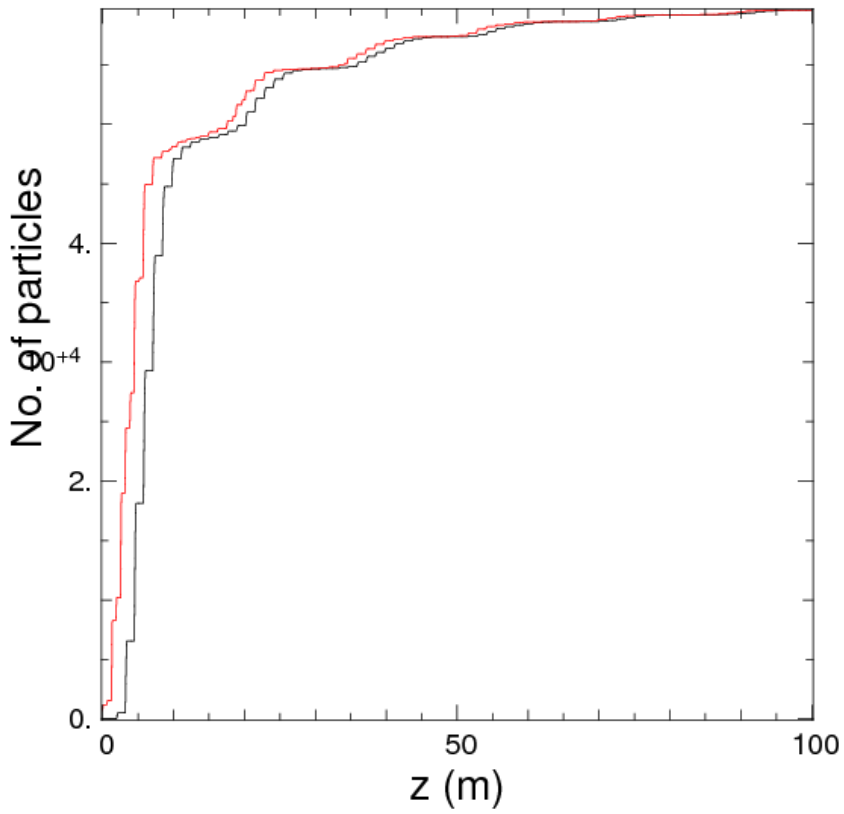

Figure 3.14: Evolution of the total number of halo particles for velocity space (red) and configuration space halo (black). Note the convergence of the two totals.

3.7 Quadrupole mode mismatch

Instead of a breathing, axisymmetric mode, we can also launch a **quadruople mismatch** mode, in which case the beam size in x, X_{rms} oscillates with a phase difference of π rads compared to the oscillations of Y_{rms}.

In Fig. 3.15 we see the $r - r'$ projection of the particle distribution (in black) as well as the halo population (in red). Since we no longer have azimuthal symmetry, the

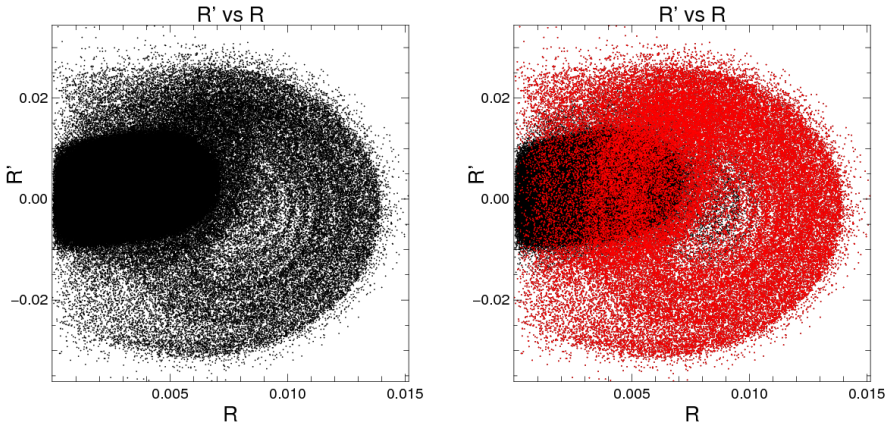

(a) $r - r'$ projection of the total particle population (b) $r - r'$ projection of the halo population (red)

Figure 3.15: Comparison of the total particle population and the halo (red)

resonance island is smeared compared to the breathing mode case.

3.8 Halo removal methods

The method most commonly used to mitigate halo is collimation, although more elaborate schemes that employ nonlinear focusing fields have been proposed [55]. During collimation, one or more apertures are used to scrape the halo particles. This process is complicated by the fact that at any specific point along the beam line, some of the halo

particles are inside the core. These particles have high velocities, and will eventually go outside the beam core, but they can obviously not be scraped.

Indeed, as we see in Fig. 3.16, collimating only the visible halo would result in eliminating only around 10% of the total halo population. Hence, collimation at a single point would result in the halo reappearing later on, to a lesser but still significant extent.

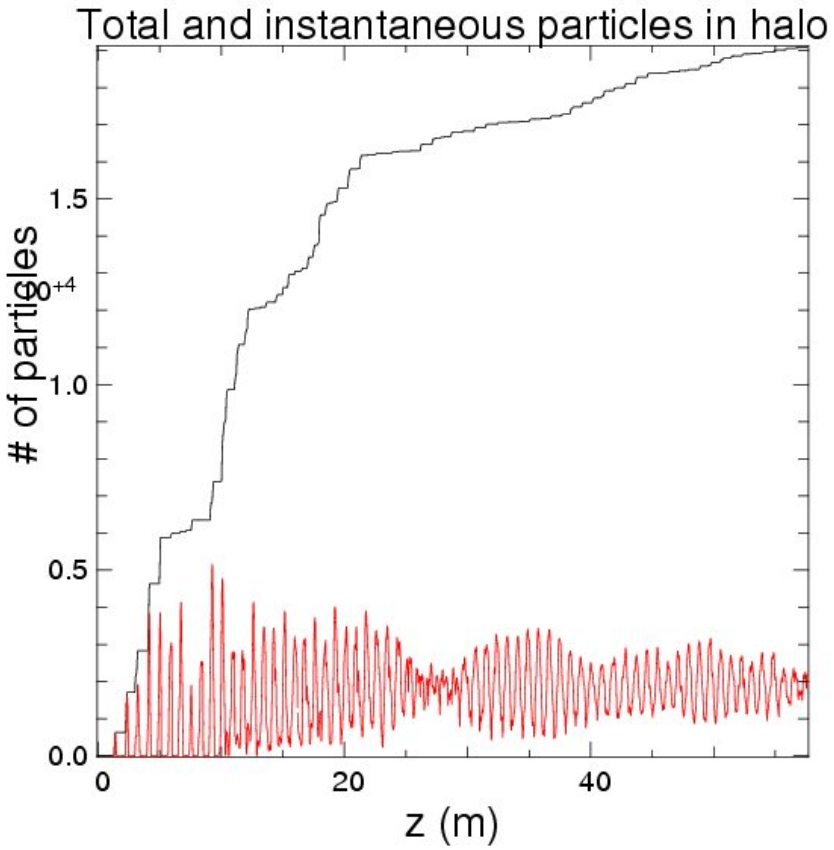

Figure 3.16: Total number of particles in the halo (black) and instantaneous number (red). At any given distance, only the red population forms the visible halo

3.8.1 Ideal collimation

In addition to the halo regeneration mechanism discussed previously, where the majority of the resonant particles are not removed when a single collimating aperture is applied, there is also the issue of new particles becoming resonant and thus reform the halo population.

In the simulations, we can apply an ideal collimator, in the sense that we can remove all particles tagged as ”halo particles”. This way, we do not only eliminate the particles that are far from the beam core, but also the halo particles that are instantaneously in the core, but have high transverse velocities and would reform the halo downstream.

We can apply this procedure in two cases, one at the beginning of the simulation, when the beam core performs oscillations and after we transport the beam for a significant distance, in which case the core oscillations have been damped. A graphical view of the procedure is given in Figs 3.17 and 3.18 for the first case and Figs 3.20 and 3.21 for the second case.

We note that in the first case, the halo is regenerated, as the core oscillations resonate with new particles. This is not a trivial point, since the new halo particles were not resonant before, but apparently have been shifted in phase space. The possibility of numerical collisions has been eliminated, since increasing the number of particles gives identical results.

We can conclude now that this phase space mixing is a collective phenomenon, due to the internal, collective space charge force. This is in agreement with earlier work on chaotic mixing in the case of intense beams and gravitational systems, as discussed in

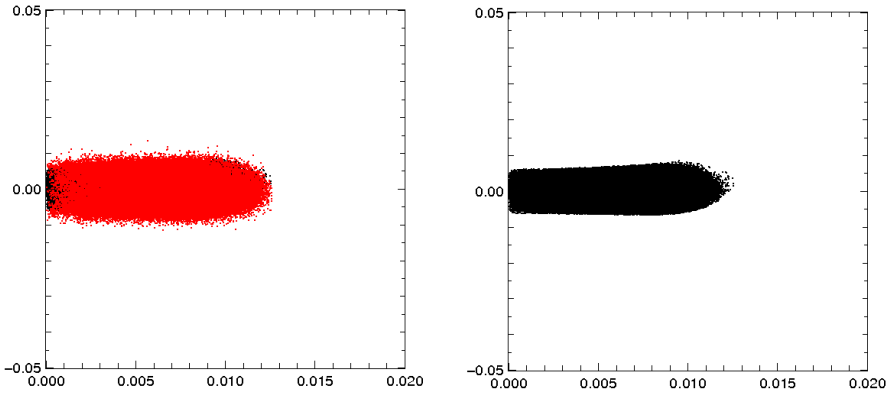

Figure 3.17: Ideal collimation of halo particles (red) in $r - r'$, at $z = 0$ m

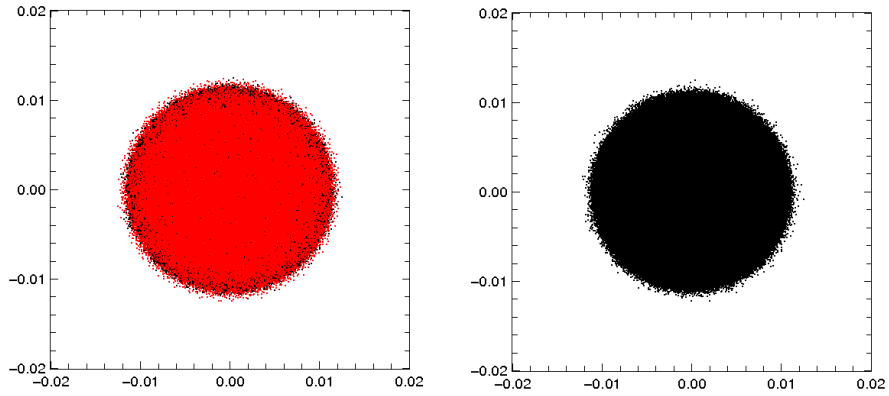

Figure 3.18: Ideal collimation of halo particles (red) in $x - y$, at $z = 0$ m

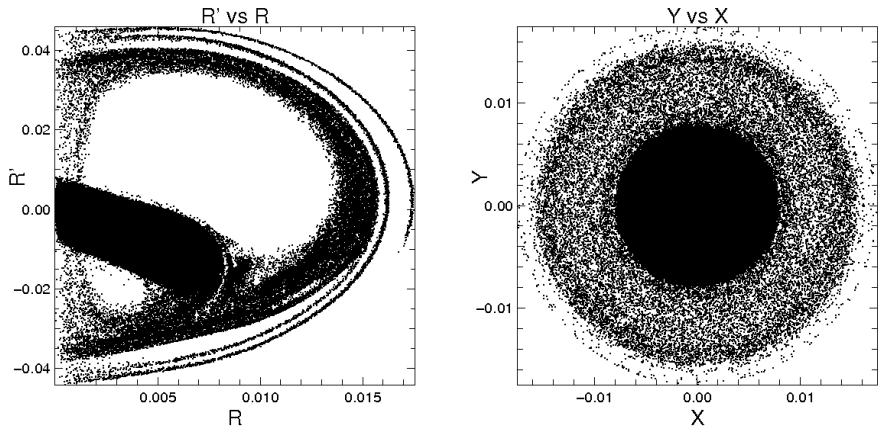

Figure 3.19: Reappearance of the halo at $z = 100\text{m} = 65\lambda_p$, after an ideal collimator is applied at $z = 0$ m. Compare with Fig. 3.11

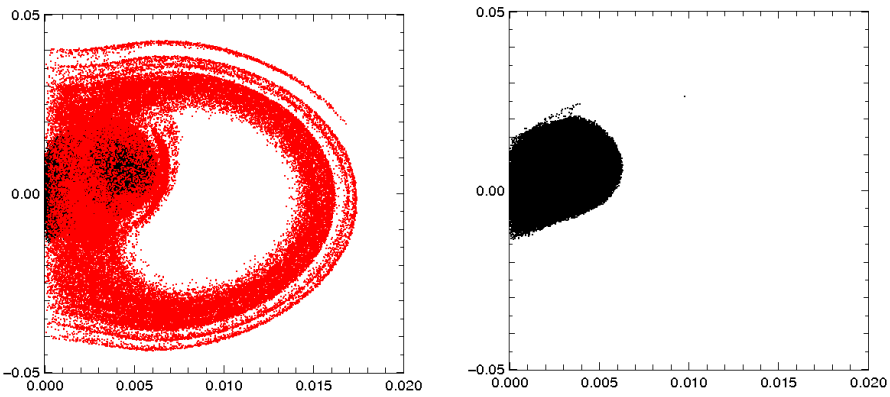

Figure 3.20: Ideal collimation of halo particles (red) in $r - r'$ at $z = 100\text{x} = 65\lambda_p$, after the beam oscillations have been damped

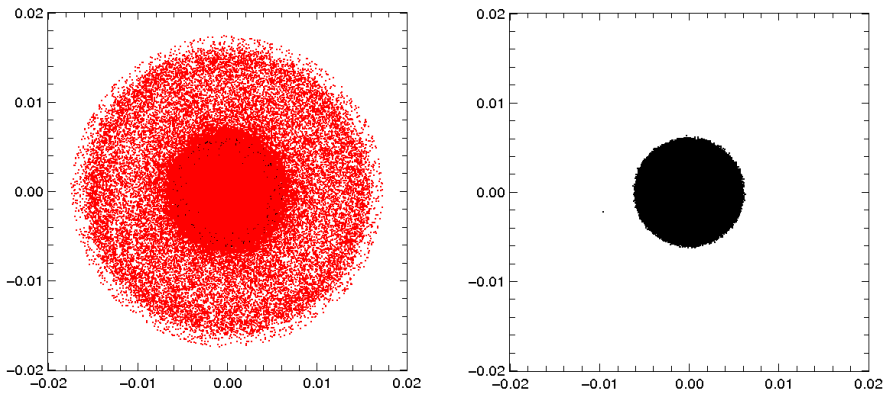

Figure 3.21: Ideal collimation of halo particles (red) in $x - y$ at $z = 100\text{x} = 65\lambda_p$, after the beam oscillations are damped

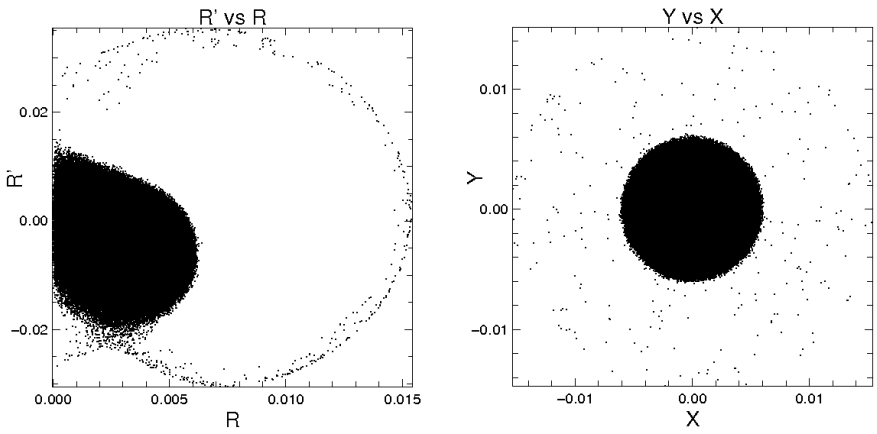

Figure 3.22: Only a small portion of the halo reappears after an ideal collimator is applied at the beginning of the run. Compare with Fig. 3.11

[56] and references therein.

On the other hand, if we apply our ideal collimation scheme after the beam has reached a steady state, the halo does not reappear, since the driving mechanism is no longer present. Although we still expect collective space charge forces to redistribute the particles, this does not lead to core oscillations, as long as the number of particles in the halo is small.

3.9 Comparison with particle-core model

As discussed in Chapter 2, the particle-core model explains halo creation in the cases we simulated through a parametric resonance mechanism. In the case of axisymmetric beams, this leads to a distinct pattern in phase space, as shown in Fig. 3.23, where we compare the particle-core model to WARP, without adjusting any parameters.

We see that in Fig. 3.23 we have very good agreement between the two simulation models in the structure of the resonance island, but not at the exact location of the resonance or the size of the beam. This is due to emittance increase in the WARP run, from 48 to 70, mm-mrad, an effect that is not included in the particle core model.

We should note first that in Fig. 3.23, the beam core oscillations have been damped, and no longer drive a parametric resonance. Nevertheless, the particles that had been pushed to the halo continue to have high transverse kinetic energies and hence they continue to perform high amplitude oscillations.

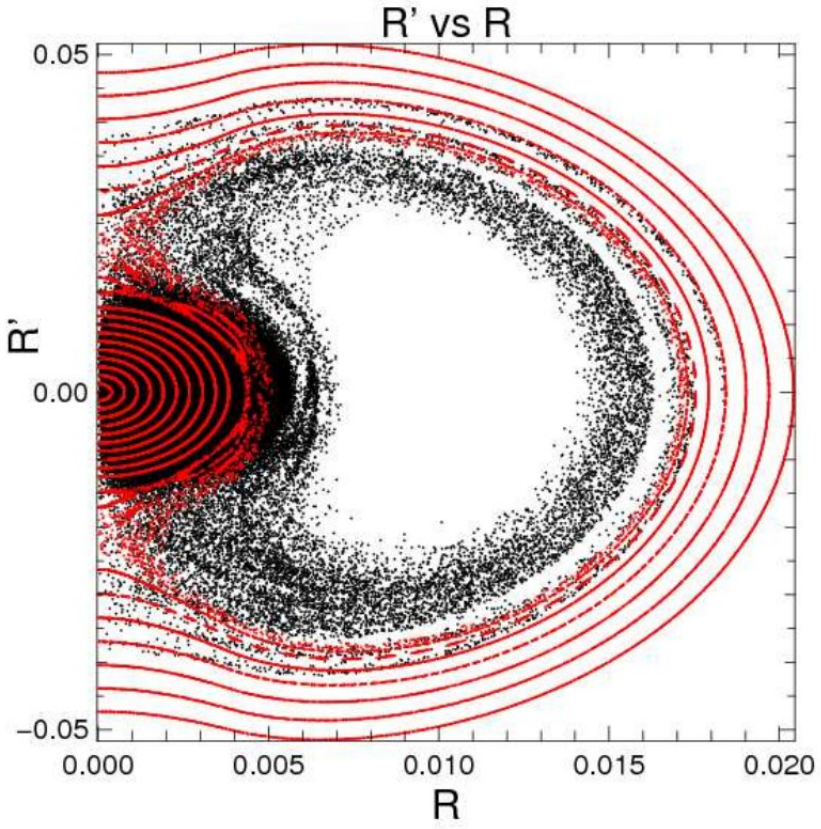

Figure 3.23: Comparison of WARP (black) and particle-core (red) phase space structure at $z = 100\text{x} = 65\lambda_p$.

3.10 Chapter Conclusion

In this Chapter we discussed the effects of initial distribution and space charge on the detailed evolution of the particle distribution function. We saw that although the emittance growth associated with halo creation is the same for the cases studied, the total number of halo particles differs. This difference is attributed to the detailed structure of the phase space within the beam core that leads to a different number of particles satisfying the parametric resonance condition necessary for halo creation. We can thus focus on the TE distribution, knowing that the qualitative features of the halo remain the same for all cases, whereas the detailed structure depends significantly on the particulars of the beam distribution and thus must be measured experimentally. In this Chapter we have compared the predictions of the particle-core model of halo creation with self-consistent PIC simulations using WARP. We see that, in the case of a mismatched beam, the predictions of the model agree with the simulations in the case of resonance structure and halo extent.

This agreement though does not hold in the important issue of halo regeneration. In particular, the effect of space charge is to mix particles in phase space and thus to push new particles into the resonance, something that cannot be modelled by the simple, linear particle-core model.

Furthermore, we were able to associate the halo in configuration $(x - y)$ space with the halo in velocity $(x' - y')$ space, and we found that the two population coincide. This has important implications for halo diagnostics that can measure the velocity distribution of a beam, such as Optical Transition Radiation.

Chapter 4

Skew Quadrupoles and Halo Creation

A realistic quadrupole transport channel, such as the one in UMER, will in general have a number of quadrupole errors, due to mechanical and electrical defects in the position and construction of the magnets. In this chapter, we will discuss the effects of one particular type of quadrupole misalignment, namely skewness, which occurs when the axes of one or more quadrupoles are not parallel to the axes defined by the rest of the transport channel. This is closely related to the case of having the frame defined by the beam axes forming an angle with the frame of the transport channel.

This kind of misalignment has been studied before in the context of intense beams. In particular, Chernin [57] was the first to derive an rms envelope equation for a beam coasting in a FODO lattice with at least one skew quadrupole. Barnard et al [58, 59] rederived the rms envelope equations and consequently discovered two new conserved quantities and a new type of oscillatory mode for the beam envelope. Building on that, Kishek et al [60] discussed the effect of small, random rotations of the quadrupoles, while Franchetti et al [61] studied the effect of the coupling between the x and y directions that is introduced by the presence of skew quadrupoles The association between beam halos and skew quadrupoles was first made by Kishek et al in [62].

In this chapter, we will discuss the effect of skew quadrupoles, or rotational mismatches, to a space charge dominated beam, in the context of halo creation. In section

4.1, we review the basic theory of beam envelope equations in a skew quadrupole channel. Section 4.2 describes a particle core model constructed to study halo creation in the presence of rotations, while 4.3 presents WARP simulations of the same case. Continuing to section 4.4 we discuss the experimental setup used, and in 4.5 we compare WARP simulations to experiments performed at UMER. Finally, the conclusions and discussion are presented in section 4.5.

4.1 Beam evolution with rotational mismatches

As discussed before, we have a skew quadrupole when the axes defined by the beam ellipse do not coincide with the planes of the quadrupole field or with the lab frame. This is shown graphically in Fig. 4.1, where the beam frame is defined by the (x_b, y_b) axes, the quadrupole frame by the (x_0, y_0) axes and the lab frame by (x, y). The angle α in Fig. 4.1

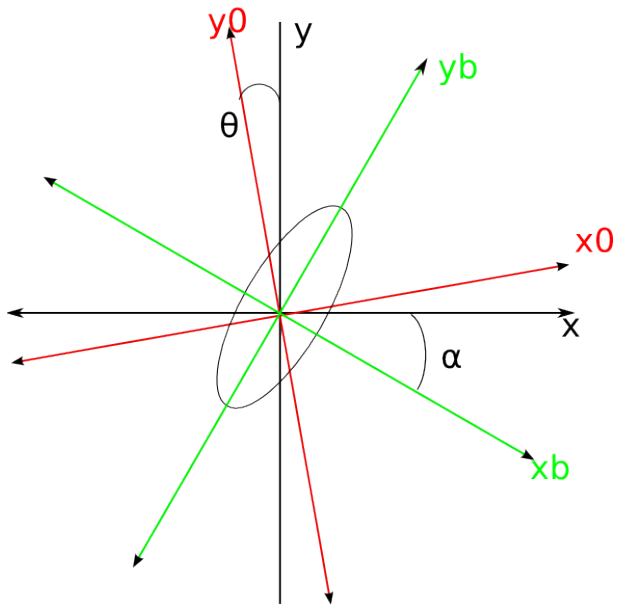

Figure 4.1: Lab frame (x, y) (black), beam frame (x_b, y_b) (green) and quadrupole frame (x_0, y_0) (red)

can be defined in terms of the beam moments in the lab frame from (4.1):

$$\alpha = \frac{1}{2} \arctan\left(\frac{2\Delta xy}{\Delta x^2 - \Delta y^2}\right) \tag{4.1}$$

where we follow the notation in [58] and the operator Δ is defined in terms of the $<>$ operator of Eq. (2.3).

$$\Delta ab = < ab > - < a >< b > \tag{4.2}$$

We note that in the case of $\Delta x^2 = \Delta y^2$, there exists an ambiguity in the definition of the angle α, as we can have either an elliptical beam with $\alpha = 45^\circ$ or a circular beam, in which case α is not defined. Because of this, special care should be taken in the numeric calculations to distinguish between the two cases.

Without going into the detailed derivations, we can write for the time evolution of the beam moments in the lab frame, under the assumption of linear space charge forces

within the beam core:

$$\frac{\mathrm{d}\Delta x^2}{\mathrm{d}z} = 2\Delta x x' \tag{4.3}$$

$$\frac{\mathrm{d}\Delta x x'}{\mathrm{d}z} = \Delta x'^2 + K_{xx}\Delta x^2 + K_{xy}\Delta x y \tag{4.4}$$

$$\frac{\mathrm{d}\Delta x'^2}{\mathrm{d}z} = 2K_{xx}\Delta x x' + 2K_{xy}\Delta x' y \tag{4.5}$$

$$\frac{\mathrm{d}\Delta y^2}{\mathrm{d}z} = 2\Delta y y' \tag{4.6}$$

$$\frac{\mathrm{d}\Delta y y'}{\mathrm{d}z} = \Delta y'^2 + K_{yy}\Delta y^2 + K_{yx}\Delta x y \tag{4.7}$$

$$\frac{\mathrm{d}\Delta y'^2}{\mathrm{d}z} = 2K_{yy}\Delta y y' + 2K_{yx}\Delta y' x \tag{4.8}$$

$$\frac{\mathrm{d}\Delta x y}{\mathrm{d}z} = \Delta x' y + \Delta x y' \tag{4.9}$$

$$\frac{\mathrm{d}\Delta x' y}{\mathrm{d}z} = \Delta x' y' + K_{xx}\Delta x y + K_{xy}\Delta y^2 \tag{4.10}$$

$$\frac{\mathrm{d}\Delta x y'}{\mathrm{d}z} = \Delta x' y' + K_{yy}\Delta x y + K_{yx}\Delta x^2 \tag{4.11}$$

$$\frac{\mathrm{d}\Delta x' y'}{\mathrm{d}z} = K_{xx}\Delta x y' + K_{xy}\Delta y y' + K_{yy}\Delta x' y + K_{yx}\Delta x x' \tag{4.12}$$

where we have used the notation in Ref. [58] and the coefficients K_{ab} are defined as follows:

$$K_{xx} = K_{qxx} + K_{sxx}$$

$$K_{xy} = K_{yx} = K_{qxy} + K_{sxy}$$

$$K_{yy} = K_{qyy} + K_{syy}$$

The K coefficients with subscript s are related to the space charge force and the rotation angle α of the beam with respect to the lab frame, whereas the K coefficients with subscript q are related to the external forces and the angle θ between the transport lattice and the lab frame. In the following, we present the expressions for all the coefficients for

completeness:

$$K_{qxx} = K_{qx0} \cos 2\theta \tag{4.13}$$

$$K_{qxy} = K_{qyx} = K_{qx0} \sin 2\theta \tag{4.14}$$

$$K_{qyy} = \begin{cases} -K_{qxx} & \text{for alternating focusing} \\ K_{qxx} & \text{for uniform focusing} \end{cases} \tag{4.15}$$

and:

$$K_{sxx} = K_{sxb} \cos^2 \alpha + K_{syb} \sin^2 \alpha \tag{4.16}$$

$$K_{sxy} = (K_{sxb} - K_{syb}) \sin \alpha \cos \alpha \tag{4.17}$$

$$K_{syy} = K_{syb} \cos^2 \alpha + K_{sxb} \sin^2 \alpha \tag{4.18}$$

The information about the external forces is contained in K_{qx0}, while the perveance K of the beam enters through K_{sxb} and K_{syb}, as shown in Eqs (4.19), (4.20) and (4.21).

$$K_{qx0} = \begin{cases} -k_{\beta 0}^2 & \text{for uniform focusing} \\ \frac{eB'}{m_e \beta c} & \text{for a magnetic quadrupole FODO lattice} \end{cases} \tag{4.19}$$

and:

$$K_{sxb} = \frac{K}{2\left(\Delta x_b^2 + \sqrt{\Delta x_b^2 \Delta y_b^2}\right)} \tag{4.20}$$

$$K_{syb} = \frac{K}{2\left(\Delta y_b^2 + \sqrt{\Delta x_b^2 \Delta y_b^2}\right)} \tag{4.21}$$

where the moments with subscript b refer to the moments in the beam frame.

Using this model, Barnard was able to derive two conserved quantities that are closely related to the emittances in x and y, and are a special case of the generalized

emittances studied by Dragt et al [63]:

$$\epsilon_g^2 = \frac{1}{2}\left(\epsilon_x^2 + \epsilon_y^2\right) + 16\left(\Delta xy\Delta x'y' - \Delta xy'\Delta x'y\right) \tag{4.22}$$

$$\begin{aligned}\epsilon_h^4 = {} & \epsilon_x^2\epsilon_y^2 + 16((\Delta xy\Delta x'y')^2 + (\Delta xy'\Delta x'y)^2 - \\ & \Delta x^2\Delta y^2(\Delta x'y')^2 - \Delta x^2\Delta y'^2(\Delta x'y)^2 - \Delta x'^2\Delta y^2(\Delta xy')^2 - \Delta x'^2\Delta y'^2(\Delta xy)^2 - \\ & 2\Delta xy\Delta xy'\Delta x'y\Delta x'y' + 2\Delta xx'\Delta y'^2\Delta xy\Delta x'y - 2\Delta xx'\Delta yy'\Delta xy\Delta x'y' - \\ & 2\Delta xx'\Delta yy'\Delta xy'\Delta x'y + 2\Delta x'^2\Delta yy'\Delta xy\Delta xy' + 2\Delta x^2\Delta yy'\Delta x'y\Delta x'y' + \\ & 2\Delta xx'\Delta y^2\Delta x'y'\Delta xy')^{\frac{1}{2}}\end{aligned} \tag{4.23}$$

From the analysis of the moment equations (4.3)-(4.12), Barnard and Losic concluded in Ref. [59] that there exist three types of oscillatory modes for the beam envelope, namely:

1. A breathing mode, where Δx^2 and Δy^2 oscillate in phase

2. Two quadrupole modes, where Δx^2 and Δy^2 oscillate with a 90° difference in phase

3. A new, low frequency, rotating mode

The stability analysis of these modes is presented in Ref. [59] and in the rest of this chapter we assume that we are within the stability limits of those modes.

4.2 Particle-core model for rotating beams

As discussed previously, the particle-core model proposes a mechanism for halo creation as a result of the parametric resonance between the beam core oscillations and individual particles' betatron oscillations. In the case of a skew beam (or equivalently a skew quadrupole), there exists a new class of envelope oscillations, due to the rotation

of the beam ellipse in transverse space. This new type of oscillation can also couple to single particle betatron oscillations, potentially leading to halo creation.

In this section, we develop an extended particle-core model that includes the effects of rotation. As discussed in Chapter 3, this will lead to a better understanding of the halo formation process, but not necessarily to a complete description, since the particle-core model is, in this case as in Chapter 3, not self consistent.

4.2.1 Electric field from an elliptical charge distribution

In order to model the effect of a uniform elliptical charge distribution to a single test particle at an arbitrary position inside and outside of the beam, we use the approach and expressions derived in Ref. [64]. The expressions are greatly simplified if we make use of complex variables, as it can be shown that in a charge free region, the electric field $\boldsymbol{E}(\boldsymbol{x})$ is a function of the complex conjugate $\bar{z}$ of the transverse position $z = x + iy$. This follows from the properties of the $\boldsymbol{E}$ field in vacuum, where:

$$\nabla \cdot \boldsymbol{E} = 0, \quad \nabla \times \boldsymbol{E} = 0 \tag{4.24}$$

$$\frac{\partial E_x}{\partial x} = -\frac{\partial E_y}{\partial y}, \quad \frac{\partial E_x}{\partial y} = \frac{\partial E_y}{\partial x} \tag{4.25}$$

Eq. (4.25) are essentially the Cauchy-Riemann equations for the E field, which means that in charge free space, $\boldsymbol{E}$ is a function of $\bar{z} = x - iy$ only.

We can now define the auxiliary complex variables $\bar{z}$ and ξ for an arbitrary point

(x_0, y_0) as follows:

$$\bar{z} = x_0 - iy_0 \tag{4.26}$$

$$\xi = \frac{x_0}{a} + i\frac{y_0}{b} \tag{4.27}$$

We can now calculate the complex field $E(\boldsymbol{x_0})$ as follows:

$$E_x + iE_y = E(\boldsymbol{x_0}) = \begin{cases} \frac{4\lambda}{a+b}\xi \\ \\ \frac{4\lambda}{\bar{z}+\sqrt{\bar{z}^2-a^2+b^2}} \end{cases} \tag{4.28}$$

where λ is the charge density of the beam, which we assume to be uniform, and the beam envelope parameters a and b can be calculated from the beam moments in the lab frame from Eqs (4.29) and (4.30):

$$a^2 = 2\Delta x^2 \tag{4.29}$$

$$b^2 = 2\Delta y^2 \tag{4.30}$$

The real fields $E_x = \mathrm{Re}\,\boldsymbol{E}$ and $E_y = \mathrm{Im}\,\boldsymbol{E}$ correspond to the x and y components of the electric field at the point (x_0, y_0).

4.2.2 Model

We now have all the equations needed to construct a generalized particle-core model along the lines of Gluckstern's model in Ref. [1] in order to better understand halo creation from skew quadrupole effects. That is, we have models that describe:

1. The rms envelope equations that describe the evolution of the beam core.

2. The electric field due to the presence of an arbitrary elliptical charge distribution, i.e. the effect of the beam envelope on a test particle.

Combining these two models, we can construct a code that calculates the evolution of the beam core, as well as the trajectories of test particles, for a FODO transport channel.

To simplify the analysis, we assume that all the quadrupoles in our transport system are well aligned, as in Ref. [62], but the beam enters the channel at some angle with respect to the quadrupoles' axes. Referring to Fig. 4.1, this is equivalent to having the angle $\theta = 0$, but the angle $\alpha \neq 0$. At every time step of the numerical integration, we save the positions and velocities of the test particle, as well as all the second order moments of the beam core. Of course, we are mostly interested in the size of the beam in x and y, namely Δx^2 and Δy^2, since the electric field that couples the core to the halo particles depends only on those moments, at least within our model.

As a first step, we plot the phase space trajectories of single particles with initial x position uniformly distributed between 0 and $3\ r_0$, and 0 initial y position and velocity. The case of 0 skew angle is shown in Fig. 4.2.

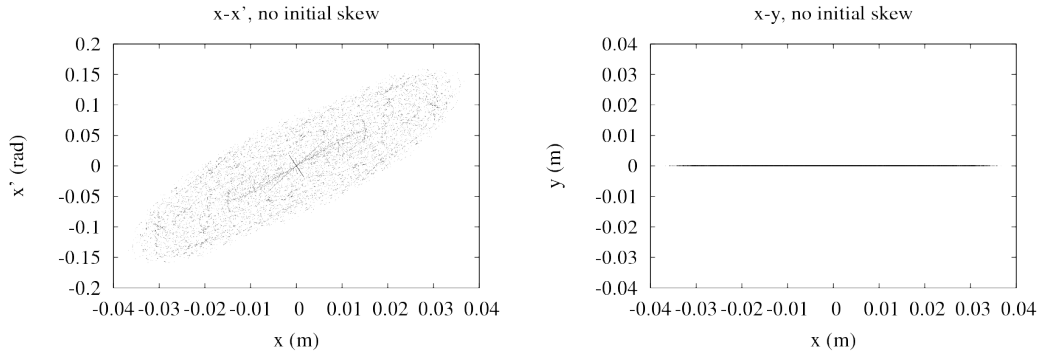

Figure 4.2: Phase space ($x - x'$) and transverse space ($x - y$) plot of a single particle trajectory for and initial beam skew of $0°$

Comparing these plots with the ones in Fig. 4.3 for an initial beam skew of $2°$ and identical initial conditions for the single particles, we see that the maximum extent of the

halo does not seem to depend strongly on the initial mismatch angle.

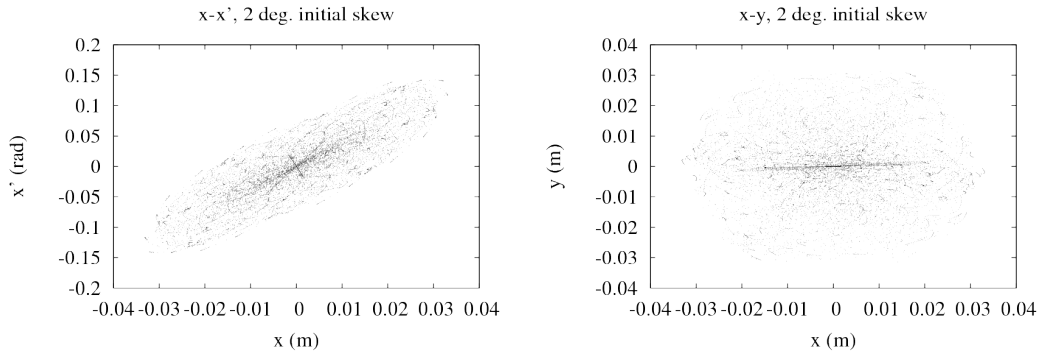

Figure 4.3: Phase space ($x - x'$) and transverse space ($x - y$) plot of a single particle trajectory for initial beam skew of 2°. Same scale as Fig. 4.2

We define the maximum halo extent at any time step as the distance from the beam center of the most distant particle, which is not necessarily the same particle throughout the simulation. It is plotted as a function of initial skew angle in Fig. 4.4, where we see that although the maximum extent of the beam halo, as predicted by the particle-core model, is a monotonically increasing function of the initial skew angle, the change is relatively small, at around 6.25% for a 10 degree skew mismatch.

4.3 Comparison of particle-core with WARP

As discussed in Chapter 3, the WARP Particle-In-Cell code is ideally suited for simulating charged particle beams in the energy and density regime relevant to the UMER parameters.

For the purpose of our simulations, we used an accurate model of UMER in WARP that includes the measured fields of the solenoid, dipole and quadrupole magnets in the transport channel, based on the `UMERGeometry` module developed by Prof. Kishek.

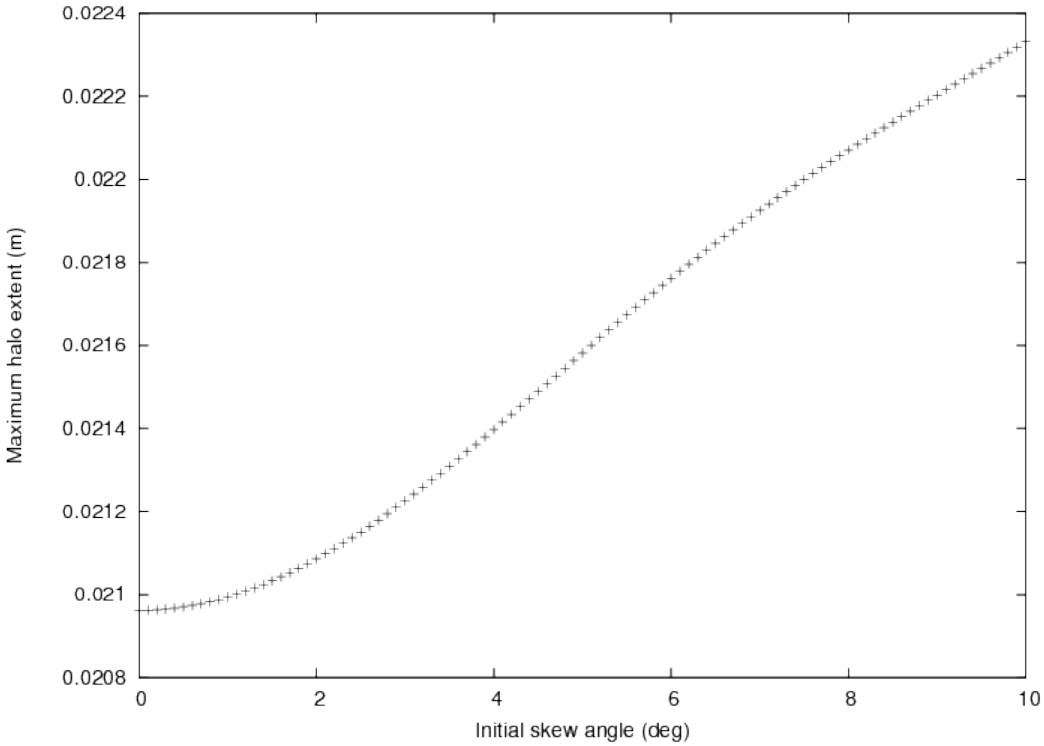

Figure 4.4: Maximum halo extent as a function of initial skew angle, prediction of the particle core model.

The skew quadrupole, which is placed at the injection quadrupole Q6, was modeled as a linear element.

In the previous section, we saw that the particle-core simulations predict a weak dependence of the halo extent on initial skew mismatch. In Fig. 4.5, we compare WARP simulations for initial skew angles of 2° and 10° degrees, plotting the beam envelope and the maximum halo extent, which is calculated at every time step and, as in the case of the particle core model, is defined as the maximum particle distance from the beam center. In Fig. 4.6, we compare the prediction of the particle-core model and WARP for the

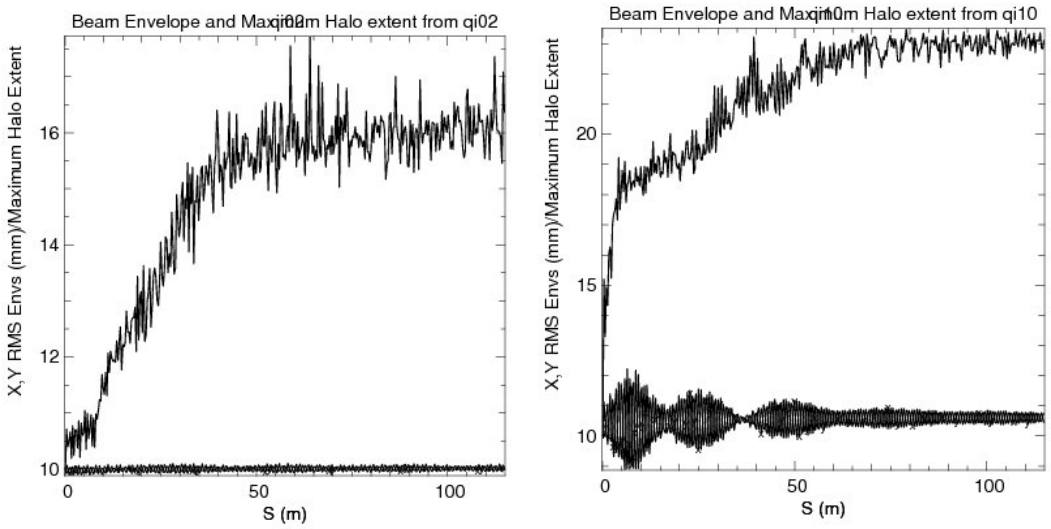

(a) Init. skew: 2° (b) Init. skew: 10°

Figure 4.5: Comparison of the maximum halo extent from WARP for 2° and 10° degrees of initial skew mismatch

maximum halo extent as well as the beam radius. As we see in Fig. 4.6, the particle-core model shows a weaker dependence of the maximum halo extent on the initial skew angle than the WARP simulations. Indeed, as we discussed earlier, the particle core model does not include effects such as emittance growth and, in this particular case, the damping of

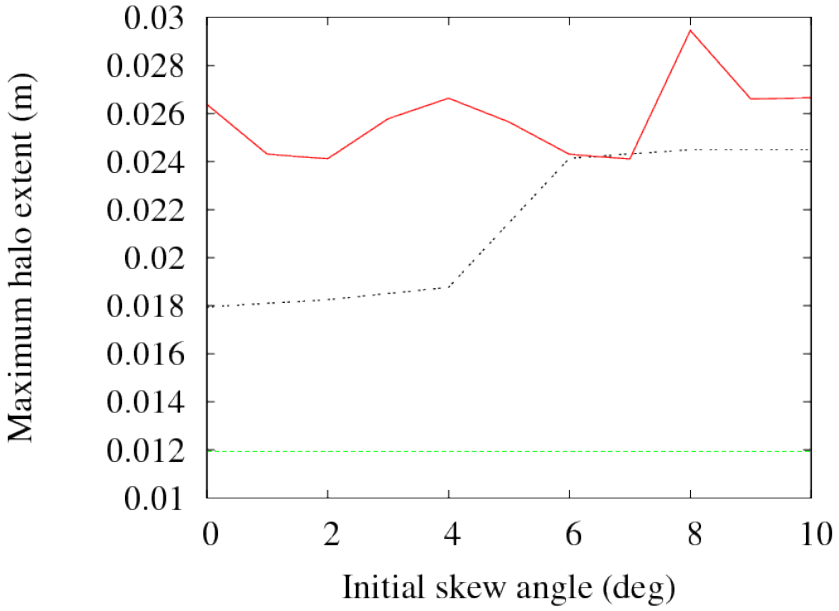

Figure 4.6: Comparison of WARP (black) and particle-core (red) prediction for the maximum extent of the halo as a function of initial skew angle, for 100 mA. The matched beam envelope radius is shown in green.

the beam rotation modes. It should be noted though, that in both cases a maximum extent is predicted and that it is 2-3 times larger than the matched beam radius.

We can thus conclude that, as was the case for the simpler particle-core model described in Chapter 3, the self-consistency of PIC simulations leads to different predictions. In this case, the differences are more significant, as the beam is perturbed even more and emittance growth is now larger.

4.4 Experimental Setup

Seeing that the comparison between simulations and the particle core model do not give satisfactory agreement, we must move to experiments, in order to check which of the

two cases is closer to reality. As discussed before, UMER provides a very good test bed for this type of studies, and indeed skew quadrupole experiments have been performed before [2], albeit for a shorter distance. In the rest of this section, we briefly describe the experimental setup we used for our measurements.

4.4.1 Phosphor screens

The simplest way to measure the transverse properties of the UMER beam is to take a picture of the beam, by using a phosphor screen. These screens are located at diagnostic chambers positioned every 64 cm along the ring.

In particular, the screens are coated with P-43 phosphor ($Gd_2O_2S:Tb$), that has a response time of 1.6 μs and a peak emission at 545 nm. The response time is much longer than the beam pulse duration of 100 ns, and thus the screen in effect integrates over the whole pulse. That is, any time dependent phenomena cannot be resolved in our case.

4.4.2 Digital camera system

In order to capture the image of the beam, we used an IMPEX charged coupled device (CCD) camera [36]. It can operate in 8- or 12-bit modes, and in the following 8-bit pictures are shown, even though the analysis of the data was done using the full, 12-bit dynamic range of the camera.

The camera has a maximum shutter frequency of 20 Hz, and hence the beam pulse frequency was reduced from the usual 60 Hz. We do not expect this to cause any difference, since the circulation time is much higher than the repetition rate.

In the case of faint beams, we had the option of integrating over multiple frames, thus linearly increasing the light intensity at each point. This is preferable to increasing the gain of the camera, as the latter procedure does not preserve the linearity as well.

4.4.3 Printed circuit skew quadrupole

In order to compare the WARP simulations with the experiment, we made use of the printed-circuit magnets that were constructed by H. Li [2]. The skew and normal components of the printed-circuit magnet are shown in Fig. 4.7 If the current I_s through

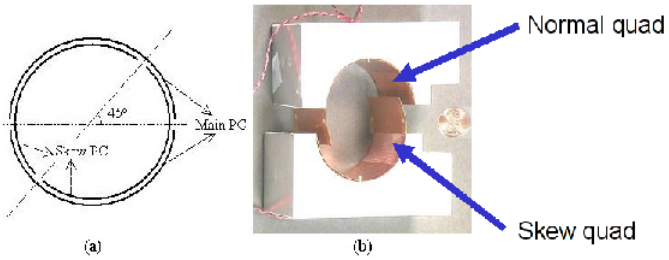

Figure 4.7: The skew and normal components of the printed circuit quadrupole. From [2]

the skew component is small compared to the current I_0 through the normal component, the field resulting from the combination of the two printed circuits is still quadrupole, but its axes are now tilted by an angle θ that can be calculated using Eq. (4.31) from Ref. [2]

$$\theta = \frac{1}{2}\arctan\left(\frac{I_s}{I_0}\right) \tag{4.31}$$

The skew quadrupole was install at Q6, the quadrupole just before the Y-section, as shown in Fig. 4.8. The normal component of Q6, corresponding to I_0 in Eq (4.31) was set to its normal operational value, while the skew component, corresponding to I_s, was connected to an independent power supply.

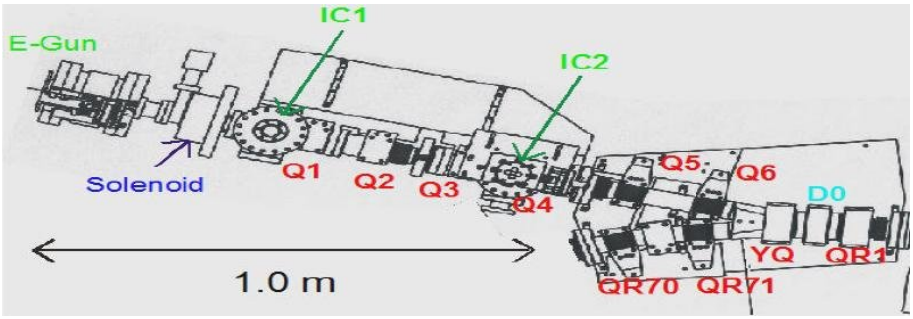

Figure 4.8: Schematic of the Y section. The skew quadrupole is placed at Q6. Courtesy of S. Bernal.

4.5 Measurements

Using the apparatus desribed in the previous section, we are able to adjust the rotation angle of the quadrupole Q6 by changing I_s. During this procedure, we can either keep I_0, the current through the normal component of the quadrupole, constant, or we can change it so as to keep a constant total current.

In the experiments, we used the 7 mA and the 23 mA beam of UMER, which were described in Chapter 2. Both beams are space charge dominated, with a χ value of 0.6 and .84 respectively.

4.5.1 Comparison with WARP simulations

In Fig. 4.9 we compare the experiment with simulations, for the 23 mA beam, at the diagnostic chamber RC1, which is located 191 cm from the source and 68 cm from the skew quadrupole. Quantitatively, the rotation angles from the experiment and the simulation are plotted in Fig. 4.10.

One of the most salient properties of the 23 mA beam in the experiment is the fact

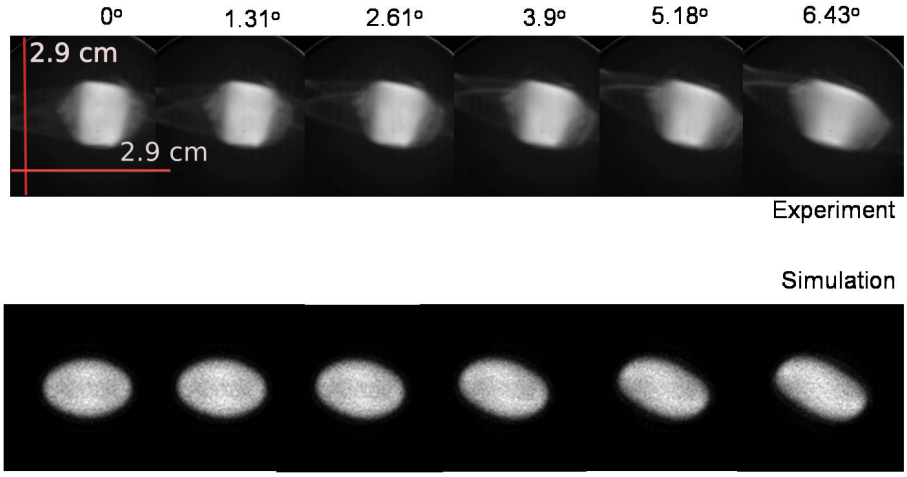

Figure 4.9: Comparison of the evolution of the 23 mA beam at RC1 between experiment and simulation for different initial skew angles.

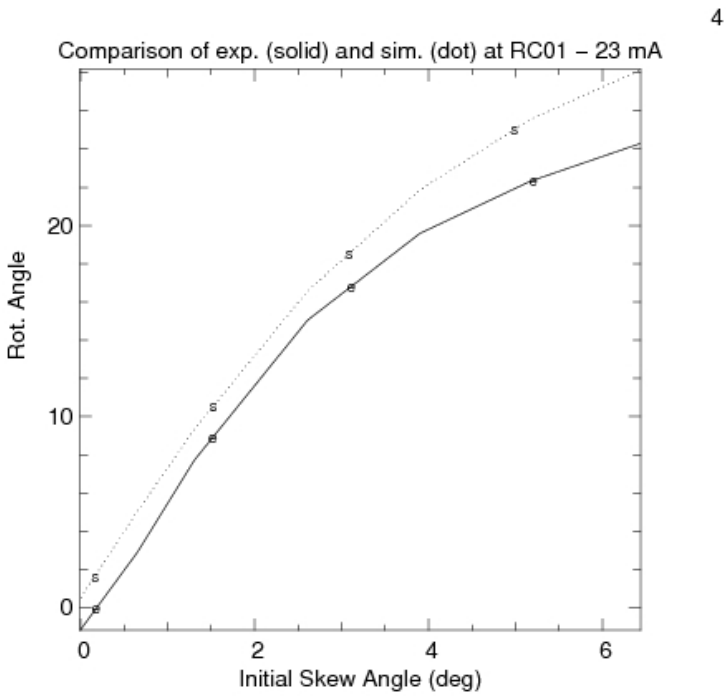

Figure 4.10: Quantitative comparison of the evolution of the 23 mA beam for the same parameters as in Fig. 4.9

that it exhibits a halo, even in the case of 0 initial skew. This can be attributed to a number of factors, such as mismatch in the injection section or halo from the gun as described in Chapter 3 [1]. The presence of an a priori halo complicates the analysis, as will be discussed later.

In experiments performed after the cathode alignment that removed the initial halo, we did indeed get a cleaner beam, as shown in Fig. 4.11 for the 7 mA beam and Fig. 4.12 for the 23 mA beam. Additionally, a switch constructed by S. Bernal was installed, allowing us to easily flip the polarity of the skew quadrupole and thus get both positive and negative rotation angles.

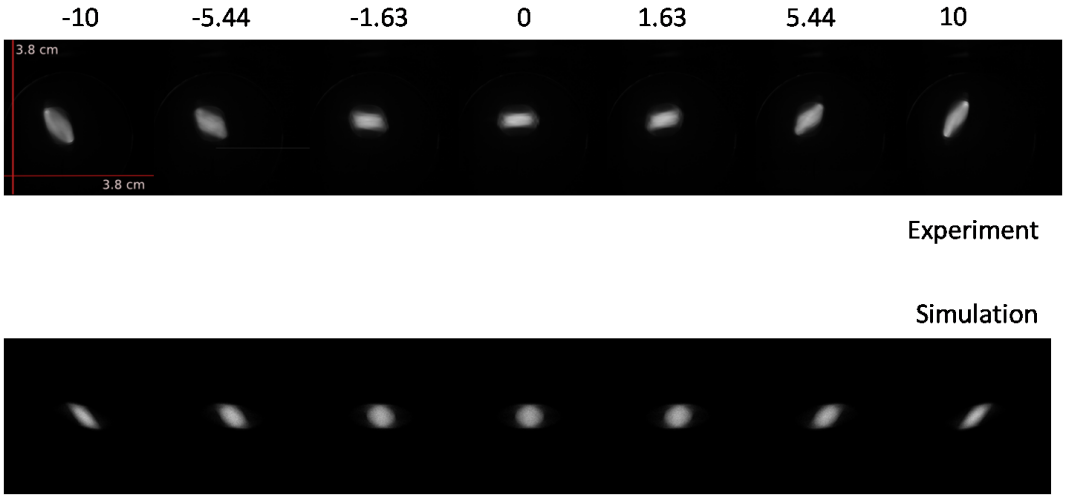

Figure 4.11: Comparison of experiment and WARP at RC1 for the 7 mA beam for different initial skew angles (above).

For the 23 mA beam, we have at the same diagnostic chamber Fig. 4.12.

Comparing Fig. 4.11 and 4.12, we see that the, qualitative, agreement between WARP and experiment is better for the smaller, lower χ beam. This is to be expected, since as we mentioned repeatedly increasing the space charge forces leads to a number of

[1] This type of halo has been removed since

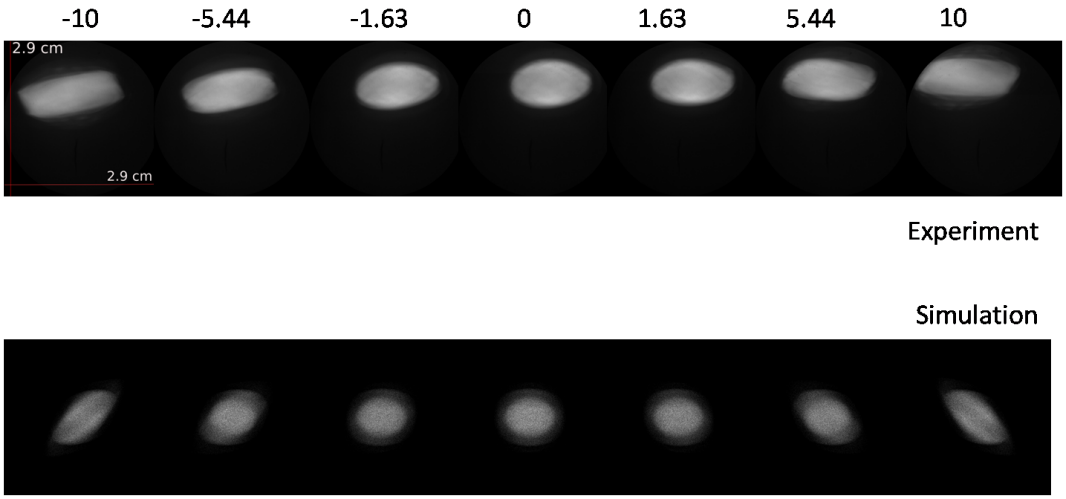

Figure 4.12: Comparison of expreriment and WARP at RC1 for the 23 mA beam for different initial skew angles (above).

complications, that are not always easy to pinpoint. The larger size of the 23 mA beam is an important contributing factor, since the beam is now closer to the beam pipe and image forces become more important.

4.5.2 Effect of initial halo

As we mentioned before, in our first experiment, the beam exhibited a halo even in the case of 0 initial skew. This can radically change the rotation of the beam, as shown in Fig. 4.13. There, we compare the experiment to WARP for 3 different initial distributions, the SG described earlier, as well as two initial distributions from self-consistent gun simulation [3]. In the first of these, the position of the cathode is such that no initial halo exists, while for the second one an initial halo is present.

As we see in Fig. 4.13, even the orientation of the beam can change due to the presence of the initial halo. Since the properties of the latter are hard to measure with the

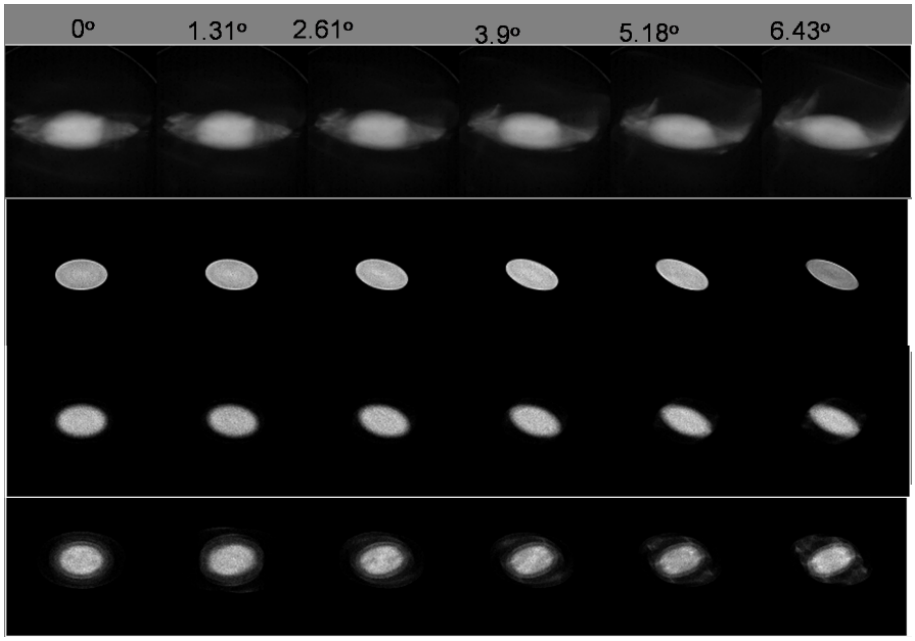

Figure 4.13: Comparison of experiment (top) and WARP simulations using a SG and two self-consistent distributions from [3]. Scale same as in Fig. 4.13. Note the different orientation of the beam in the case of the third simulation.

current diagnostics, it is very difficult to accurately model the rotation of the beam for this case.

4.5.3 Effect of Image Forces

Since the pipe containing the charged particle beam is in general a conductor, image forces arise, as is described in numerous books. These forces are especially important in the case of intense beams, and also when the beam is off-centered [27]. In the latter case, the image forces can break the symmetry of the system, severely affecting the shape of the beam.

Although WARP incorporates image force effects, comparing them to experiment is difficult, since we do not always have the diagnostic capability to measure the centroid of

the beam and thus deduce how off-centered the beam is. This is particularly problematic at the Y-section, where the injector line connects to the ring at an angle, and the beam centroid does not coincide with the center of the quadrupole field there.

As shown in Fig. 4.14, the symmetry of the beam is broken in the experiment, most likely due to image forces, but the structure of the beam halo shows similarities with the halo observed in WARP simulations.

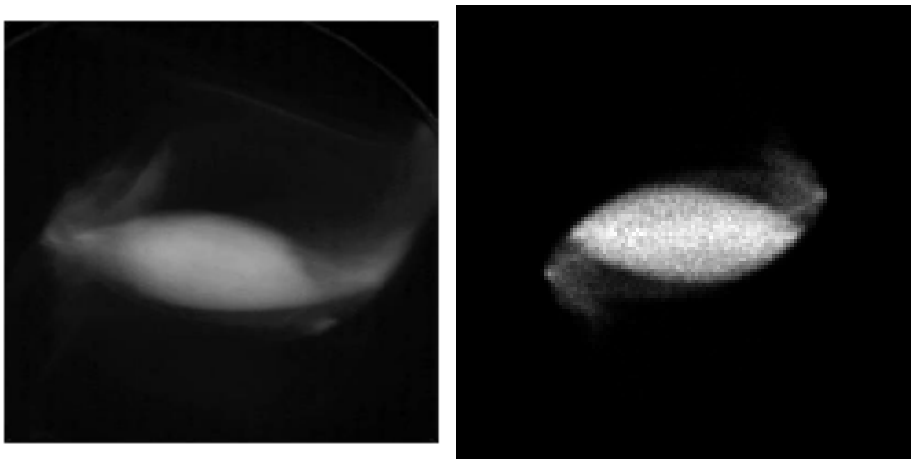

(a) Experiment (b) Simulation

Figure 4.14: Comparison of experiment and simulation at RC3 for an initial skew angle of $6.43°$. Note the lack of symmetry in the experimental case.

4.5.4 Effect of nonlinear forces on the halo

As shown in both the simulations and the experiment, the halo produced in the case of skew quadrupoles has a distinct spiral structure or filamentation. This filamentation, colloquially referred to as ”s-ing”, is widely known in the case of phase space and is associated with nonlinear forces, either due to space charge or magnet nonlinearities [27].

In the case of skew quadrupoles, we see from Eq. 4.28 that even in the case of a

uniform ellipse, the space charge force at an arbitrary point outside the beam ellipse is nonlinear in x and y, while inside the ellipse the space charge force is linear. Hence, to a first approximation, the effect of a skew quadrupole on the beam core is a rotation and a scaling, but not a filamentation.

On the other hand, the particles in the halo experience a differential rotation under the combined effect of the linear, rotated quadrupole field and the nonlinear space charge field. This leads to spiral structures, observed both in simulations and experiments.

4.5.5 Damping of the oscillatory modes

In Fig. 4.15, we see the comparison between warp and experiment at RC6 (5.1 m from the source and

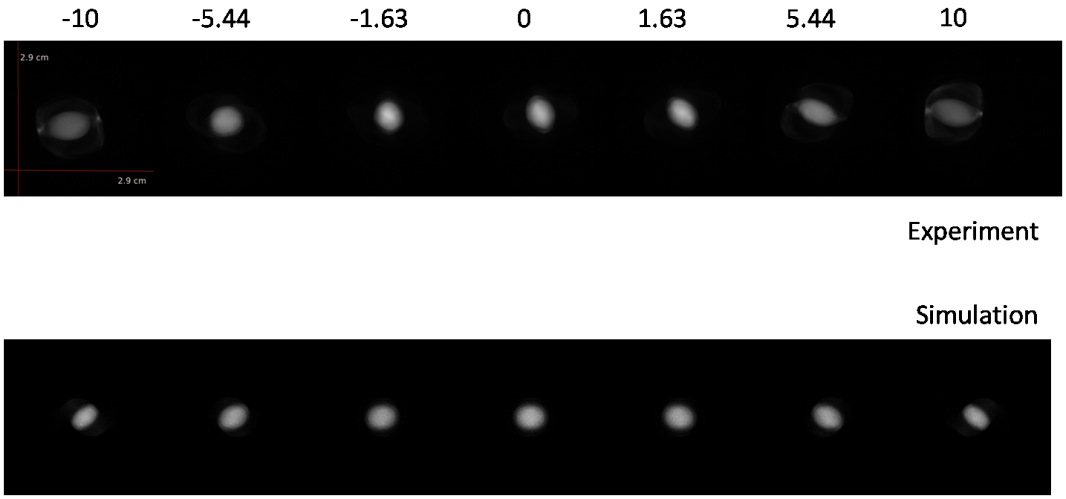

Figure 4.15: Comparison between experiment and WARP at RC6. Note that the orientation of the beam core changes little in both cases, while the halo structure changes significantly

4.6 Chapter Conclusion

In Chapter 5, we investigated the creation of halo due to a skew mismatch. For this purpose, we employed both a modified particle-core model, as well as WARP simulations. The prediction of the former that there is a weak dependence of the halo maximum extent on the initial skew angle is confirmed by WARP Comparison with WARP showed good agreement for the two cases, withing the constraints discussed in Chapter 3.

Furthermore, we presented measurements of beam rotation angles and halo from the UMER ring. The experimental data was compared to WARP simulations. It was also compared for a longer distance than before, as well as for different polarities of the skew quadrupole.

Chapter 5

Conclusion

5.1 Summary

The goal of this research project has been to better understand the creation of halo in intense charged particle beams. As discussed in Chapter 1, the emergence of halo can significantly deteriorate beam quality, as well as hinder the continuous and safe operation of accelerator facilities. The need to address this issue becomes even more urgent in the case of intense beams, since in general they create more halo particles.

Although in most of the thesis we discussed electron beams, the same phenomena are expected to appear in all stable particle beams that are sufficiently intense. Indeed, the basic equations of Chapter 2 are identical for the two cases, as the relevant parameter is the intensity parameter χ, instead of the current or the beam energy. We discussed the question of rigorously defining a halo, as well as the particle-core model that postulates a parametric resonance between collective oscillations of the beam core and resonant particles as the mechanism for halo creation.

The effect of different initial distributions was discussed in Chapter 3, where we confirmed earlier work that showed a correlation between beam mismatch, chaotic or intermittently chaotic trajectories and halo creation. Furthermore, we saw that, although the type of the beam distribution does not affect the gross features of the halo in the 4-dimensional phase space, the number of particles that are captured by the parametric

resonance depends on the details of the phase space structure within the beam core.

We also compared the particle-core model with PIC simulations using the WARP code. The lack of self-consistency of the first model became apparent, since it could not account for the re-emergence of halo particles after their removal in the simulations. Furthermore, we saw in the simulations strong evidence that the halo populations in $x - y$ and $x' - y'$ coincide, an observation with important implications for halo diagnostics.

In Chapter 4 we constructed a particle-core model to account for possible rotations of the beam in an alternating gradient focusing channel due to skew quadrupoles. This new model was then compared to WARP simulation and we were able to derive The main result of this was the observation that in that case of rotational mismatches, the beam halo is distorted due to the nonlinear forces outside the beam core. Experiments at the University of Maryland Electron Ring showed good agreement, within the constraints of experimental error.

5.2 Future Work

As discussed in Chapter 3, the halo can appear both in configuration and velocity space, and the WARP simulations indicate that the two populations coincide. This hypothesis can be tested experimentally for energies in the MeV range using phase space diagnostic methods such as Optical Transition Radiation Interferometry [65] or Phase Space Tomography [36], that allow us to simultaneously measure the velocity and spatial distribution of the beam. A variety of methods have been proposed to increase the dynamic range of these diagnostics in order to better measure the halo [66], and preliminary

studies have been proposed for the University of Maryland Electron Ring.

On the theory and simulation front, a better understanding of the effects of the beam distribution will be possible once an equilibrium distribution for a FODO channel is constructed. This way, we will not have to rely on simple, uniform charge distributions to calculate the space-charge force on halo particles, but we will have a more accurate description of the coupling force, which will likely include additional nonlinear effects.

On the issue of collimation and halo mitigation in general, we must note that ensuring good magnet alignment and matching remains the best way to minimize halo. Removing the halo in the case of space charge dominated beams is more complicated than in the case of emittance dominated beams. This is due to the collective effects within the beam core in the first case that force new particles in the halo, even when the original halo has been completely removed. Hence, controlling the halo requires a very accurate description of both the beam and the external forces acting on it.

Appendix A

Correspondence between plasmas and intense beams

As discussed before, it is sometimes useful to think of intense beams as non-neutral plasmas [34, 27]. Indeed, a number of quantities familiar from neutral plasmas can be defined for intense beams. The formulas connecting the quantities in the two cases are simplest for a matched beam coasting at constant speed in a smooth focusing channel, and in this Appendix we will follow this convention. Hence, we can define a transverse temperature for the beam, which is closely related to the beam emittance:

$$k_B T_{x,y} = \gamma m \left\langle v_{x,y} \right\rangle^2 = \gamma m \frac{\epsilon^2}{a^2} \tag{A.1}$$

where ϵ is the beam emittance and a the beam radius.

The phenomenon of Debye shielding is also present in charged particle beams, and the characteristic Debye length is given by Eq. (A.2).

$$\lambda_D = \gamma \left(\frac{\pi \epsilon_0 \beta c^3 \epsilon}{4 q^2 I} \right)^{\frac{1}{2}} \tag{A.2}$$

We should note that although the Debye length is defined in the same way, in the case of non-neutral plasmas the exponentially decaying electric field associated with Debye screening is added to the total electric field due to the like charges. Hence, the range of internal space charge forces is larger than λ_D.

The sound speed is again defined similarly to neutral plasma theory, and is given in

Eq. (A.3).

$$c_s^2 = g\frac{q^2 I}{4\pi\epsilon_0 m\beta c\gamma^5} \tag{A.3}$$

where the geometric factor g is related to the beam size and the radius of the beam pipe. The sound speed is the speed at which space charge waves travel along the beam.

Additionally, for low energies, radiation effects are minimal, in contrast to high energy machines. Hence, the system is Hamiltonian, since the energy losses due to synchrotron or other types of radiation are very small. Indeed, since the radiated energy scales with γ^4, the number of photons emitted in the regime of low energies is minimal.

In that case, the collisionless Vlasov equation [34] is given in Eq. (A.4)

$$\frac{\partial f}{\partial t} + \boldsymbol{v}\frac{\partial f}{\partial \boldsymbol{x}} + \frac{q}{m}\left(\boldsymbol{E} + \boldsymbol{v}\times\boldsymbol{B}\right)\frac{\partial f}{\partial \boldsymbol{v}} = 0 \tag{A.4}$$

It should be noted that although there is a close connection between plasmas and intense beams, there are a few important differences. Most apparent is the fact that beams are **non-neutral** and hence a number of the assumptions of classical plasma physics do not hold.

More subtly, the existence of **long range forces** in non-neutral plasmas complicates the statistical mechanics of beam physics. In particular, there does not exist a true thermodynamical equilibrium described by a Maxwell-Boltzmann distribution, but rather a stationary state, where average quantities are stationary, but detailed balance is violated [67, 68].

Appendix B

The WARP Particle-In-Cell Code

WARP [69] is a particle-in-cell (PIC) code, developed at Lawrence Berkeley and Lawrence Livermore National Labs. It is ideally suited for the study of intense charged particle beams, and has been benchmarked extensively for the case of ion beams [70] as well as low energy electron machines such as UMER [3, 71].

The WARP base libraries are written in Fortran or C, in order to optimize the performance of the code, but they are accessed at a higher level through Python. This gives a lot of flexibility to the code, as well as the testing advantages of an interpreted language such as Python.

The base libraries of WARP are complemented with routines that implement a number of the distributions discussed in the thesis. Additionally, graphics libraries are available for the visualization of the simulations.

Furthermore, through Python we have the ability to access a wide variety of useful numerical routines through the `Numeric` or `SciPy` modules of Python, which are open source and vectorized for maximum efficiency.

The WARP code incorporates different models of the beam, in particular a full 3-dimensional case as well as two separate 2-dimensional approximations, the **slice** code, useful in the case of simulations related to the physics of transverse phenomena and the **r-z** code, which is used in azimuthally symmetric geometries if we are interested in lon-

gitudinal phenomena as well. In all of those cases, the electrostatic fields calculated by the code are self-consistent, withing the appropriate model.

As noted before, since we mostly dealt with transverse physics, we used the slice code. In this case, all the particles are propagated from an initial position in z, z_i to a final position z_f. Hence, the propagation time is not the same across the beam, as the velocity v_z is in general different for each particle.

Although not used in our case, it should be noted that WARP can also be used in parallel mode, taking advantage of multiple processors.

B.0.1 Sample WARP Code

In the following, we present a sample input file, also known as "deck", for the WARP code that implements both the tracking of tracer clumps of particles described in Chapter 3, as well as the tagging of halo particles according to the definition of Eq. 3.4. The deck was adapted from a sample deck provided by Prof. R. Kishek.

```
#       Saves the particles that have radius > halo_radius at any
#       point in their history
#       Additionaly, dumps all particles before the first step so that
#       the core file can be used in another simulation
#       Also tracks 5 clumps of low current, used as tracers
#
#       smooth focusing
#
#   The FFT Solver is used, and f3d.a capacity matrix is used
#   to specify a cylindrical boundary.
#

from warp import *
import sys
sys.path.insert(1, "/work/papadopc/myscripts")
# if 'GISTPATH' in os.environ.keys():
#     os.environ["GISTPATH"] += ":/ebte/pywarp/rscripts/scripts_a"
# else:
#     os.environ["GISTPATH"] = "/ebte/pywarp/rscripts/scripts_a"
from my_rami_match import *
from my_rami_scripts import *
```

```
from monitor import *
from tomo_photos import *
from particles import _setindices

ldebug = no
createmonitor(passwd = "papadopc$job", port = 50021)

lppxy_snap = no
print_maxextent = no
print_particles_in_halo = yes
print_kurtosis = yes


halo_radius = [1.5,1.6,1.7,1.8,1.9]
#halo_radius = [2.0]
if ldebug:
    lmatch = yes          # 2 period matching -- ALSO Change titles
    lpicts = no             # Take density pictures?
else:
    lmatch = no          # 2 period matching -- ALSO Change titles
    lpicts = yes            # Take density pictures?

kappa = 10.0

zlen = 100.0
############## RUN   CONDITIONS ################

rand_type = "Gauss"     # Type of random errors "Gauss" or "Uniform"
plot_distrib = no       # Plot Error distribution?

save_all = yes          # Save at every time step?
lcalc_mom = no          # Calculate additional moments?
lfilt =  not lpicts     # Filtering?
if lpicts: from mphoto import *

lmatch_env = no      # Matching with ENV code

# --- Set four-character run id, comment lines, user's name.

top.runid  = 'big_mis'
runid = arraytostr(top.runid)
top.pline2 = "dz=0.4 cm, nx=ny=2*256"
top.pline1 = "5 TURNS; REL2; 'hele' quads; NO_SYMM; fstype=1;\
 Gauss FILT"
top.runmaker = "Chris Papadopoulos"

# --- Comparison

lcompare = no
#dot1 = "rq00"        # Compare against
#crun = "0"           # Run number


# --- Invoke setup routine (THIS IS MANDATORY)
```

```
setup()


############ B E A M   P A R A M E T E R S ###############

sfact = 1.0     # Factor by which beam SIZE is divided
swall = 1.0     # Wall scaling factor

top.pgroup.ns = 6       # Number of clumps
top.ns=6
# Colors associated with each clump
colors = ["fg", "red", "blue", "green", "magenta", "cyan"]
gchange("*",0)

# --- Set beam Parameters.  Note that ibeam is negative for electrons.

# calculate unnormalized emittance
# nemit       = 50.0e-6*top.clight/top.vbeam
top.emitx_s[0]       = 40.0e-6/(sfact**2)
top.emity_s[0]       = 40.0e-6/(sfact**2)


top.ibeam_s[0]      = - 23.0e-03/(sfact**2)
# Calculate matched beam radius
init_ibeam=top.ibeam_s[0]

rel_gamma=1+10./511.
rel_beta=sqrt(1-1/rel_gamma**2)

I0 = 4.*pi*top.eps0*top.emass*top.clight**3/top.echarge
gen_perv = abs(init_ibeam/I0*2./(rel_gamma*rel_beta)**3)
u = gen_perv/(2.*sqrt(kappa)*top.emitx_s[0])
a0_matched = sqrt(top.emitx_s[0]/sqrt(kappa))*sqrt(u+sqrt(1.+u**2))
top.a0_s[0]=1.5*a0_matched
top.b0_s[0]=top.a0_s[0]
top.ap0_s[0]=0.0
top.bp0_s[0]=0.0
top.ekin_s       = 10.0e03
top.aion_s       = top.emass/top.amu
top.zion_s       = -1.
top.lrelativ  = yes       #  pushes particles relativistically.



# --- Clump parameters

Delt = 1./10.0
Epsil = 1./100.0

xDelta = top.a0_s[0]*Delt      # Offset of beamlet centroid relative
#to certain positions
xEpsil = top.a0_s[0]*Epsil     # Size of beamlet
xAngle = top.emitx_s[0]/top.a0_s[0]     # Maximum angle at waist
```

```
yDelta = top.b0_s[0]*Delt      # Offset of beamlet centroid relative
#to certain positions
yEpsil = top.b0_s[0]*Epsil     # Size of beamlet
yAngle = top.emity_s[0]/top.b0_s[0]     # Maximum angle at waist

# --- Set test clump (perturbation) Parameters.
top.a0_s[1:top.pgroup.ns]     = xEpsil
top.b0_s[1:top.pgroup.ns]     = yEpsil
top.ap0_s[1:top.pgroup.ns]    = top.ap0*Epsil
top.bp0_s[1:top.pgroup.ns]    = top.bp0*Epsil
# Weight of perturbation parts
top.ibeam_s[1:top.pgroup.ns] = top.ibeam_s[0]*(Epsil**4)
top.ekin_s[1:top.pgroup.ns]  = top.ekin_s[0]
top.aion_s[1:top.pgroup.ns]  = top.aion_s[0]
top.zion_s[1:top.pgroup.ns]  = top.zion_s[0]

top.emitx_s[1:top.pgroup.ns] = top.emitx_s[0]*(Epsil**2)
top.emity_s[1:top.pgroup.ns] = top.emity_s[0]*(Epsil**2)

# --- Clump 1 -- Near Edge, with zero angle

top.xcent_s[1]  = top.a0_s[0] - xDelta
top.ycent_s[1]  = 0.0
top.xpcent_s[1] = 0.0
top.ypcent_s[1] = 0.0

# --- Clump 2 -- Near Edge, with OUTWARD angle

top.xcent_s[2]  = 0.0
top.ycent_s[2]  = top.b0_s[0] - yDelta
top.xpcent_s[2] = 0.0
top.ypcent_s[2] = yAngle

# --- Clump 3 -- Near mid-Beam, with zero angle

top.xcent_s[3]  = -(top.a0_s[0] - xDelta)/2.0
top.ycent_s[3]  = 0.0
top.xpcent_s[3] = 0.0
top.ypcent_s[3] = 0.0

# --- Clump 4 -- Near Center, with zero angle

top.xcent_s[4]  = 0.0
top.ycent_s[4]  = - yDelta
top.xpcent_s[4] = 0.0
top.ypcent_s[4] = 0.0

# --- Clump 5 -- Near Middle, at some angle

top.xcent_s[5]  = 0.5*top.a0_s[0]
top.ycent_s[5]  = 0.75*top.b0_s[0] - yDelta
top.xpcent_s[5] = 0.5*xAngle
top.ypcent_s[5] = 0.75*yAngle
```

```
# The call to derivqty calculates some beam parameters,
# eg. top.vbeam from ekin.
derivqty()

#if (top.lrelativ):
#     rel_gamma = 1 + top.echarge*top.ekin/(top.emass*(clight**2))
#     rel_beta = sqrt(1-(1/rel_gamma)**2)
#     top.vbeam_s = rel_beta*clight
#     top.ibeam_s = top.ibeam_s/(rel_gamma**2)



# --- Adjust parameters for a Non-uniform beam density
# 0 --> uniform density, 2 --> hollowed density
w3d.hollow = 0
# n(w3d.rho)  not  1 + ((1-h)/h)*w3d.rho**2
w3d.hollow_h = 0.5
if (w3d.hollow == 2):
    # --- form factor for parabolic density profile
    Stf = sqrt( (2.*w3d.hollow_h+4.)/(3.*w3d.hollow_h+3.) )
    # --- scale loading parameters so the correct rms values are loaded
    top.a0_s[0] = top.a0_s[0]/Stf
    top.b0_s[0] = top.b0_s[0]/Stf
    top.ap0 = top.ap0/Stf
    top.bp0 = top.bp0/Stf
    top.emit = top.emit/Stf


# calculate a longitudinal thermal velocity corresponding to e_spread.
e_spread = 10.0           #  Longitudinal energy spread in eV
top.vthz_s      = top.vbeam*e_spread/(2.*top.ekin)
top.vtilt_s     = 0.
top.allspecl  = 0



##################### GEOMETRY & GRIDDING ######################

# +++ Boundaries
# Remove particles outside of Pipe radius
top.prwall = pr1 = swall*2.45e-2
boxrad = 2.5e-2                          # Box 1/2 side > pr1
w3d.xmmin = w3d.ymmin = -swall*boxrad           # Set box size
w3d.xmmax = w3d.ymmax =  swall*boxrad

# +++ Symmetry & Gridding

w3d.l4symtry = 0      # "1" automatically sets  xmmin = ymmin = 0
w3d.l2symtry = 0
# MUST be a POWER of 2 for FFT solver
w3d.nx = w3d.ny = nint(swall*256)
if w3d.l2symtry: w3d.ny = w3d.nx/2
```

```
# +++ Particles

# num particles per slice
top.np_s[0]     = swhere(lpicts, 1000000, 20000)
top.np_s[1:top.pgroup.ns]=50000
top.npmax=top.np_s[0]
#w3d.distrbtn = "K-V"        # load KV distribution
#w3d.distrbtn = "semigaus"  # load semi-Gaussian distribution
w3d.distrbtn = "TE"
w3d.xrandom  = "digitrev"  # load x,y,z with digitreverse random
    numbers
w3d.vtrandom = "pseudo"     # load vx, vy with pseudo random numbers
w3d.vzrandom = "pseudo"     # load vz with pseudo random numbers
w3d.ldprfile = "polar"      # load on stream lines

top.stickyxy = 1         # remove particles when they hit pipe.
# set type of pusher to  vXB push without tan corrections
top.ibpush   = 1
# +++ Stepsize
dzz = swhere(lmatch, 0.002, 0.004)       # cell size, in m
nrun = nint(zlen/dzz)            # number of time steps to take - total
top.dt = dzz/top.vbeam                   # OK, 0 injection
#wxy.lvzchang = 1    # If 1, fancy algorithm is used to find top.dt

# +++ Define geometry


# Assume that the halo extent is equal to the distance
#from the center of the particle farthest away
maxextent=zeros(nrun+1, 'd')
particles_in_halo=zeros([len(halo_radius),nrun+1])
total_particles_in_halo=zeros([len(halo_radius),nrun+1])
particles_in_halo_set=zeros([len(halo_radius),top.np_s[0]])

kurtosis_x=zeros(nrun+1, 'd')
kurtosis_y=zeros(nrun+1, 'd')

def calc_maxextent():
        current_maxex=max(getx()**2+gety()**2)
        maxextent[top.it]=sqrt(current_maxex)
        return

def calc_particles_in_halo():
        particle_radius = sqrt((top.pgroup.xp/(2.*top.xrms[0,0]))**2+\
        (top.pgroup.yp/(2.*top.yrms[0,0]))**2)

        for jj in arange(0,5):
                particles_in_halo_set[jj]=\where(less(halo_radius[jj],\
                particle_radius),1,particles_in_halo_set[jj])
                total_particles_in_halo[jj,top.it]=\
                sum(particles_in_halo_set[jj])

        return
```

```
def calc_kurtosis():
        kurtosis_x[top.it] = (sum(top.pgroup.xp**4)/top.nplive)\
        /(sum(top.pgroup.xp**2)/top.nplive)**2-2.
        kurtosis_y[top.it] = (sum(top.pgroup.yp**4)/top.nplive)\
        /(sum(top.pgroup.yp**2)/top.nplive)**2-2.
        return

def plot_maxex(runid=None,  kwdict={}, **kw):
    """ plot_maxex(runid=None, kwdict={}, **kw)
        Plots maximum extent of the halo, using gen_plot
    """
    pldef = {'nwin': 0,'yscale': 2.e3}
    # Override defaults & import new params
    pldef.update(kwdict);  pldef.update(kw)
    try:                gen_plot(("hmaxextent", ), "zscale", None, \
    pldef, nwin=None)
    except NameError:   gen_plot(("maxextent", ), "zscale", None, \
    pldef, nwin=None)

def plot_particles_in_halo(runid=None,  kwdict={}, **kw):
    """ plot_maxex(runid=None, kwdict={}, **kw)
        Plots number of particles in the halo, using gen_plot
    """
    pldef = {'titlet':"Number of Halo particles:total and per snapshot"
       }
    # Override defaults & import new params
    pldef.update(kwdict);  pldef.update(kw)
    try:                gen_plot(("hparticles_in_halo", \
    "htotal_particles_in_halo"), "zscale", runid, pldef, nwin=None)
    except NameError:   gen_plot(("particles_in_halo", \
    "total_particles_in_halo"), "zscale", runid, pldef, nwin=None)

def plot_kurtosis(runid=None,  kwdict={}, **kw):
    """ plot_maxex(runid=None, kwdict={}, **kw)
        Plots number of particles in the halo, using gen_plot
    """
    pldef = {'titlet': "Kurtosis in x,y", }
    # Override defaults & import new params
    pldef.update(kwdict);  pldef.update(kw)
    try:                gen_plot(("hkurtosis_x", "hkurtosis_y"),\
     "zscale", runid, pldef, nwin=None)
    except NameError:   gen_plot(("kurtosis_x","kurtosis_y" ),\
     "zscale", runid, pldef, nwin=None)

def my_local_plot_env(runid=None,  kwdict={}, **kw):
    """ plot_env_maxex(runid=None, kwdict={}, **kw)
        Plots ENVS in x and y, using gen_plot and the maximum extent \
        of the halo
    """
    pldef = {'nwin': 0, 'marks': 1, 'yscale': 2.e3,
             'titlel': "X,Y RMS Envs (mm)/Maximum Halo Extent",\
              'titlet': "Beam Envelope and Maximum Halo extent from"}
             # Override defaults & import new params
```

```
    pldef.update(kwdict);  pldef.update(kw)
    try:    gen_plot(("hxrms", "hyrms"), "zscale", runid, pldef,\
    yscale=2.e3)
    except NameError:
        gen_plot(("xenv", "yenv"), "zscale", runid, pldef, yscale=2.e3)

################### F I E L D  DESCRIPTION ###################

# ---- set up lattice quantities

top.dedr = (kappa*(top.vbeam**2))*(rel_gamma*top.emass/top.echarge)
gchange("Lattice",0)



############### ENVELOPE CODE PARAMETERS ####################

env.zl=0.
env.zu=top.tunelen
env.dzenv=(env.zu-env.zl)/500

if (lmatch_env):
    # --- calculate envelope solution and plot it.
    package("env"); generate(); step()
    penv()

    env.sig_desr = 10.0
     # simple averaging between initial and final values
    env_match.match1(20)
    top.a0;top.b0;top.ap0;top.bp0
    penv()

################## S O L V E R ####################

# --- Set up Capacity Matrix for WARPxy

# Filtering
# This cutoffs off the shorter wavelengths, reducing
# the effective resolution by ~ a factor of 2
# I don't know how sensitive things are to the sharpness.
if (lfilt):
    w3d.filt[2,0:2] = 0.5    #  0.5 for Gaussian; pi/(nx/64) for Dave
    w3d.filt[3,0:2] = 2.0    #  2.0 for Gaussian; 8.0 for Dave

symm_fact = swhere( w3d.l4symtry, pi/2.0, \
swhere(w3d.l2symtry, pi, 2.0*pi) )

# --- Select Field Solver

top.fstype = 1
#                0       FFT Field Solver
#                1       FFT Solver w/ Capacity Matrix (inifinite)
#                2       FFT Solver w/ Capacity Matrix (periodic)
#                3       SOR Field Solver
```

```
if (top.fstype == 1):
    fxy.ncxy    = fxy.ncxymax = w3d.nx+w3d.ny    # set number of points
    gallot("CapMatxy",0)                         # Allocate the arrays
    # -- Coordinates in meters
    fxy.xcond[0:fxy.ncxy] = pr1*cos(symm_fact*arange(fxy.ncxy)/fxy.ncxy
        )
    fxy.ycond[0:fxy.ncxy] = pr1*sin(symm_fact*arange(fxy.ncxy)/fxy.ncxy
        )
    fxy.vcond[0:fxy.ncxy] = 0.e0                 # Put pipe at ground

f3d.lcndbndy = true      # enable subgrid interpolation


############### D I A G N O S T I C S #################

# --- Set up some windows.
zpicts = dzz + (zlen/100.0)*arange(0,100)
nd_locs = nint(array(zpicts)/dzz)
scale = 10000.e0/top.np_s[0]
if (scale > 1.e0): scale = 1.0e0
top.zwindows[:,0] = [-dzz*scale/2.0,dzz*scale/2.0]
top.rwindows[:,1] = [0.e0, 0.005e0]

top.xpplmin = top.ypplmin = -.10
top.xpplmax = top.ypplmax = 0.10

# --- Select plot intervals, etc.
top.nhist = 1
top.itplps = top.itplfreq = top.itmomnts = -1
top.itplps[0:4]=[0,nrun,nrun, 0]       # At end of run
top.itplfreq[0:4]=[0,nrun,nrun/4, 0]
top.itmomnts[0:4] = [0,1000000,abs(top.nhist),0]

# --- Select plots
top.iptrace[0] = always


###############  G E N E R A T E   ##################

#Generate the PIC code (allocate storage, load ptcls, t=0 plots, etc.)
#raise(" ")
package("wxy"); generate()

boxrad = 2.5e-2                              # Box 1/2 side > pr1

xplmin = yplmin = -boxrad
xplmax = yplmax =boxrad

peak_beam = 25.0e-3      # Maximum beam size for photos
def snapshot():
    if (top.it in nd_locs):
        loc_string = "%06d" % (1000.0*top.zbeam)
        #take_photo(peakx=peak_beam, peaky=peak_beam)
```

```
        rg = ppxxp(0, cellarray=1,\
         pplimits=(xplmin, xplmax, yplmin, yplmax),
                        xmin=-1.16*boxrad , xmax=1.16*boxrad , \
                        ymin=-1.16*boxrad , ymax=1.16*boxrad ,
                        nx=299,ny=299,ctop=255, returngrid=1)
        pname = runid+loc_string+'xxp'+'.tif'
        save_tif(rg[0],pname)
        os.system('convert -flip %s %s'%(pname, pname))

        rg = ppxy(0, cellarray=1, \
        pplimits=(xplmin, xplmax, yplmin, yplmax),
                        xmin=-1.16*boxrad , xmax=1.16*boxrad , \
                        ymin=-1.16*boxrad , ymax=1.16*boxrad ,
                        nx=299,ny=299,ctop=255, returngrid=1)
        pname =  runid+loc_string+'xy'+'.tif'
        save_tif(rg[0],pname)
        os.system('convert -flip %s %s'%(pname, pname))

        rg = ppyyp(0, cellarray=1, \
        pplimits=(xplmin, xplmax, yplmin, yplmax),
                        xmin=-1.16*boxrad , xmax=1.16*boxrad ,\
                         ymin=-1.16*boxrad , ymax=1.16*boxrad ,
                        nx=299,ny=299,ctop=255, returngrid=1)
        pname =  runid+loc_string+'yyp'+'.tif'
        save_tif(rg[0],pname)
        os.system('convert -flip %s %s'%(pname, pname))

        rg = ppxpyp(0, cellarray=1, \
        pplimits=(xplmin, xplmax, yplmin, yplmax),
                        xmin=-1.16*boxrad , xmax=1.16*boxrad , \
                        ymin=-1.16*boxrad , ymax=1.16*boxrad ,
                        nx=299,ny=299,ctop=255, returngrid=1)
        pname = runid+loc_string+'xpyp'+'.tif'
        save_tif(rg[0],pname)
        os.system('convert -flip %s %s'%(pname, pname))

        for spec in range(0,top.pgroup.ns):
                pprrp(js=spec,color=colors[spec])
        fma()

        for spec in range(0,top.pgroup.ns):
                pptrace(js=spec,color=colors[spec])
        fma()
# Take phase space snapshot
ltomo_photos = yes

if ltomo_photos:
        tomo_photos = tomo_photos_class()
        tomo_photos.nx = 256
        tomo_photos.ny = tomo_photos.nx
        tomo_photos.xmin = -0.02
        tomo_photos.xmax = 0.02
        tomo_photos.ymin = tomo_photos.xmin
        tomo_photos.ymax = tomo_photos.xmax
```

```
        tomo_photos.plot_list = ["xy","xxp","yyp","xpyp"]
        tomo_photos.subslope_plot_list = ["xxp","yyp"]
        def take_tomo_photos():
                tomo_photos.photos_locs = nd_locs
                if (top.it in tomo_photos.photos_locs):
                        tomo_photos.take_photos()

#if lpicts: installafterstep(snapshot)
#installafterstep(snapphasespc)
#installafterstep(take_tomo_photos)
def ppxy_snaphsot():
    if (top.it in nd_locs):
        nx=ny=50;
        fma()
        ppxy(color='density',chopped=0.4);
        fma()



if lpicts: installbeforestep(snapshot)
if lppxy_snap: installbeforestep(ppxy_snaphsot)
installafterstep(make_nice_output)
calc_maxextent()
installafterstep(calc_maxextent)
calc_particles_in_halo()
installafterstep(calc_particles_in_halo)
calc_kurtosis()
installafterstep(calc_kurtosis)

############### P A R T I C L E  SIMULATION ##################

stime = wtime()

top.verbosity = 1   # Turn off oneliner output.
outfile = open(runid+"_out","w")

dump() # To be used in the next simulation

#raise(" ")

if not lmatch:
    for istep in range (1, nrun+1, top.nhist):
        step(top.nhist)
        make_nice_output(0,outfile)
else:
    for istep in range (1, nrun+1):
        step()
        make_nice_output(0,outfile)

dump()

etime = wtime()
print "Time Running = ", etime-stime
```

```
################### S A V E  D A T A ####################

top.lenhist = top.jhist
gchange('Hist')

def_vars1 = ["hpnum", "hvzbar", "hvzrms",
             "hxrms", "hyrms", "hepsx", "hepsy", "hxbar", "hybar"]
def_vars2 = ["zscale", "nx", "ny", "xmmax", "ymmax"]

def_vars =  def_vars1 + def_vars2

local_vars = ["maxextent","particles_in_halo","total_particles_in_halo"
    \
,"particles_in_halo_set","kurtosis_x","kurtosis_y"]

exec "hmaxextent"+runid+'= maxextent'
exec "hparticles_in_halo"+runid+'= particles_in_halo'
exec "htotal_particles_in_halo"+runid+'= total_particles_in_halo'
exec "hparticles_in_halo_set"+runid+'= particles_in_halo_set'
exec "hkurtosis_x"+runid+'= kurtosis_x'
exec "hkurtosis_y"+runid+'= kurtosis_y'

if lcalc_mom:
    calc_mom()
    save_long(crun="0")
else:
    save_data(crun="0",vars=def_vars)            # script that saves
        data

local_vars = ["maxextent","particles_in_halo","total_particles_in_halo"
    ,\
"particles_in_halo_set","kurtosis_x","kurtosis_y"]

outfile=PW.PW("my_data_"+runid+".pdb")
import __main__
for vname_save in (local_vars):
        __main__.__dict__[vname_save+runid]=eval(vname_save)
        outfile.write(vname_save+runid,\
        eval(vname_save+runid,__main__.__dict__))
outfile.close()


###################### P L O T S ######################

begin  = 0
strobe = 1
nstpp = 1
plot_env(begin=begin,strobe=strobe); fma()
my_local_plot_env(begin=begin,strobe=nstpp)
plot_maxex(begin=begin,strobe=nstpp); fma()
plot_emit(begin=begin,strobe=strobe);   fma()

plot_env(yscale=4.0/(top.a0+top.b0),
```

```
          titlel="a/a_i", titleb="s/S");       fma()
plot_emit(yscale=2.0/(top.emitx+top.emity),
           ymin=0.0, ymax=2.5, titlel="emit/emit_i", titleb="s/S")
           fma()
plot_np();       fma()

#plot_particles_in_halo(begin=begin,strobe=nstpp); fma()
plot_kurtosis(begin=begin,strobe=nstpp); fma()

#################### C O M P A R E ########################

if (lcompare):
    plot_comp(runs={dot1+crun: {'type': "dot"}}, titlet=cf_title,
                      begin=begin, strobe=strobe)

if (print_maxextent):
        maxex_file=open("z-maxextent"+runid+".dat","w")
        ii=0;
        exec "zscale=zscale"+runid
        while ii < len(maxextent):
                out_string=str(zscale[ii])+'\t'+str(maxextent[ii])+'\n'
                maxex_file.write(out_string)
                ii+=1
        maxex_file.close()
```

Bibliography

[1] Robert L. Gluckstern. Analytic model for halo formation in high current ion linacs. *Phys. Rev. Lett.*, 73(9):1247–1250, 1994.

[2] H. Li, S. Bernal, R. A. Kishek, T. Godlove, P. G. O'Shea, and M. Reiser. Printed-circuit magnets for the university of maryland electron ring (umer) - new developments. In *Proceedings of the 2001 Particle Accelerator Conference, Chicago*, 1999.

[3] I. Haber, S. Bernal, R. A. Kishek, P. G. O'Shea, C. Papadopoulos, M. Reiser, R. B. Feldman, D. Stratakis, M. Walter, and J. L. Vay. Measurement and simulation of source-generated halos in the university of maryland electron ring (umer). In *IEEE Particle Accelerator Conference, 2007. PAC*, pages 3564–3566, 2007.

[4] L. Evans. The Large Hadron Collider. *New J. Phys*, 9:335, 2007.

[5] B. Barish, M. Ross, N. Walker, and A. Yamamoto. ILC research and development plan for the technical design phase, 2008.

[6] M. Harrison, T. Ludlam, and S. Ozaki. RHIC project overview. *Nuclear Inst. and Methods in Physics Research, A*, 499(2-3):235–244, 2003.

[7] R. R. Wilson. The Tevatron. *Phys. Today*, 10:23–30, 1977.

[8] Accelerators and Beams: Tools of Discovery and Innovation. Published by the Division of Physics of Beams of the American Physical Society.

[9] M. S. Turner. Accelerators and Dinosaurs. *Physics Today*, 56(9), 2003.

[10] C. A. Perez and L. W. Brady. Principles and practice of radiation oncology. *JNCI Cancer Spectrum*.

[11] J. N. Galayda. The advanced photon source. In *Proceedings of the Particle Accelerator Conference*, volume 1, 1995.

[12] J. B. Murphy, J. Bengtsson, R. Biscardi, A. Blednykh, L. Carr, W. Casey, S. Chouhan, S. Dierker, E. Haas, R. Heese, et al. NSLS II: The future of the NSLS. In *Particle Accelerator Conference, 2005. PAC 2005. Proceedings of the*, pages 3345–3347, 2005.

[13] R. Tatchyn, J. Arthur, M. Baltay, K. Bane, R. Boyce, M. Cornacchia, T. Cremer, A. Fisher, S. J. Hahn, M. Hernandez, et al. Research and development toward a 4.5-1.5 ă Linac Coherent Light Source (LCLS) at SLAC. *Nuclear Instruments and Methods in Physics Research Section A*, 375, 1996.

[14] M. Altarelli, R. Brinkmann, M. Chergui, W. Decking, W. Dobson, S. Düsterer, G. Grübel, W. Graeff, H. Graafsma, J. Hajdu, et al. XFEL: The European X-Ray Free-Electron Laser. Technical report, DESY, 2006.

[15] R. L. Kustom. An overview of the spallation neutron source project. *Arxiv preprint physics/0008212*, 2000.

[16] G. S. Bauer. Physics and technology of spallation neutron sources. *Nuclear Instruments and Methods in Physics Research Section A: Accelerators, Spectrometers, Detectors and Associated Equipment*, 463(3):505–543, 2001.

[17] National Research Council Committee on a Scientific Assessment of Free-Electron Laser Technology for Naval Applications. *Scientific Assessment of High-Power Free-Electron Laser Technology*. The National Academies Press, 2009.

[18] Virtual National Lab for Heavy Ion Fusion. `http://hif.lbl.gov/`.

[19] D. Kehne, M. Reiser, and H. Rudd. Experimental studies of emittance growth due to initial mismatch of a space charge dominated beam in a solenoidal focusing channel. In *Proceedings of the 1991 Particle Accelerator Conference*, pages 248–250, 1991.

[20] J. M. Lagniel. On halo formation from space-charge dominated beams. *Nuclear Instruments and Methods in Physics Research-Section A Only*, 345(1):46–53, 1994.

[21] T. P. Wangler, K. R. Crandall, R. Ryne, and T. S. Wang. Particle-core model for transverse dynamics of beam halo. *Phys. Rev. ST Accel. Beams*, 1(8):084201, 1998.

[22] C. K. Allen, K. C. D. Chan, P. L. Colestock, K. R. Crandall, R. W. Garnett, J. D. Gilpatrick, W. Lysenko, J. Qiang, J. D. Schneider, M. E. Schulze, R. L. Sheffield, H. V. Smith, and T. P. Wangler. Beam-halo measurements in high-current proton beams. *Physical Review Letters*, 89(21):214802, 2002.

[23] R. D. Ryne and J. Qiang. Large-scale simulation of beam dynamics in high intensity ion linacs using parallel supercomputers. In Alexander W. Chao., editor, *Linac 2000, Proceedings of the XXth International Linac Conference held 21-25 August, 2000 in Monterey, CA.*, volume 561, 2000.

[24] Massanori Ikegami. Particle-core analysis of mismatched beams in a periodic focusing channel. *Physical Review E*, 59(2):2330–2338, 1998.

[25] Ji Qiang, Robert D. Ryne, and Ingo Hofmann. Space-charge driven emittance growth in a 3d mismatched anisotropic beam. *Phys. Rev. Lett.*, 92(17):174801, Apr 2004.

[26] John David Jackson. *Classical Electrodynamics*. Wiley, 3rd edition, 1998.

[27] Martin Reiser. *Theory and Design of Charged Particle Beams*. Wiley-VCH, 2nd edition, 2008.

[28] A. J. Dragt. Lectures on nonlinear orbit dynamics. In *AIP Conference proceedings*, volume 87, page 147, 1982.

[29] Henry E. Kandrup, Ioannis V. Sideris, and Courtlandt L. Bohn. Chaos and the continuum limit in charged particle beams. *Phys. Rev. ST Accel. Beams*, 7(1):014202, Jan 2004.

[30] R. B. Fiorito and D. W. Rule. Optical transition radiation beam emittance diagnostics. In *AIP Conference Proceedings*, pages 21–21. IOP INSTITUTE OF PHYSICS PUBLISHING LTD, 1994.

[31] J. D. Lawson, P. M. Lapostolle, and R. L. Gluckstern. Emittance, entropy and information. *Part. Accel.*, 5:61–65, 1973.

[32] J. Struckmeier. Concept of entropy in the realm of charged particle beams. *Physical Review-Section E-Statistical Physics Plasma Fluids Related Interdiscpl Topics*, 54(1):830–837, 1996.

[33] Patrick G. O'Shea. Reversible and irreversible emittance growth. *Phys. Rev. E*, 57(1):1081–1087, Jan 1998.

[34] R. C. Davidson. *Physics of Nonneutral Plasmas*. World Scientific, 2001.

[35] J. Zhou, K. R. Samokhvalova, and C. Chen. Adiabatic thermal equilibrium theory for periodically focused axisymmetric intense beam propagation. *Physics of Plasmas*, 15:023102, 2008.

[36] Diktys Stratakis. *Tomographic Measurement of the Phase Space Distribution of a Space-Charge-Dominated Beam*. PhD thesis, University of Maryland, College Park, 2008.

[37] D. Kehne. Apertures in the umd 10 kv electron gun. Technical report, UMER, 1998.

[38] Ed Ott. *Chaos in Dynamical Systems*. Cambridge University Press, 2nd edition, 2002.

[39] C. K. Allen and T. P. Wangler. Beam halo definitions based upon moments of the particle distribution. *Phys. Rev. ST Accel. Beams*, 5(12):124202, Dec 2002.

[40] M. Dorf, R. Davidson, and E. Startsev. New spectral method for halo particle definition for intense charged particle beams. In *American Physical Society, 49th Annual Meeting of the Division of Plasma Physics, November 12-16, 2007*, 2007.

[41] William H. Press, Saul A. Teukolsky, and William T. Vetterling. *Numerical recipes: the art of scientific computing*. Cambridge university press, 3rd edition, 2007.

[42] H. Yoshida. Construction of higher order symplectic integrators. *Phys. Lett. A*, 150(5-7):262–268, 1990.

[43] C. K. Birdsall and A. B. Langdon. *Plasma physics via computer simulation*. Taylor & Francis Group, 2004.

[44] C. L. Bohn and I. V. Sideris. Chaotic orbits in thermal-equilibrium beams: Existence and dynamical implications. *Physical Review Special Topics-Accelerators and Beams*, 6(3):34203, 2003.

[45] A. Friedman and S. P. Auerbach. Numerically induced stochasticity. *Journal of Computational Physics*, 93(1):171–188, 1991.

[46] R. L. Gluckstern. Oscillation modes in two dimensional beams. In *Proceedings of the 1970 Proton Linear Accelerator Conference, Batavia, IL.* CONF-700929–(Vol. 2), Univ. of Massachusetts, Amherst), 1970.

[47] S. M. Lund and R. C. Davidson. Warm-fluid description of intense beam equilibrium and electrostatic stability properties. *Physics of Plasmas*, 5:3028, 1998.

[48] Steven M. Lund and Boris Bukh. Stability properties of the transverse envelope equations describing intense ion beam transport. *Phys. Rev. ST Accel. Beams*, 7(2):024801, Feb 2004.

[49] Steven M. Lund and Boris Bukh. Influence of conducting plate boundary conditions on the transverse envelope equations describing intense ion beam transport. *Phys. Rev. ST Accel. Beams*, 7(6):064201, Jun 2004.

[50] Steven M. Lund, John J. Barnard, Boris Bukh, Sugreev R. Chawla, and Sven H. Chilton. A core-particle model for periodically focused ion beams with intense space-charge. *Nuclear Instruments and Methods in Physics Research Section A: Accelerators, Spectrometers, Detectors and Associated Equipment*, 577(1-2):173–185, 2007. Proceedings of the 16th International Symposium on Heavy Ion Inertial Fusion - HIF 06.

[51] I. Haber, S. Bernal, C. M. Celata, A. Friedman, D. P. Grote, R. A. Kishek, B. Quinn, P. G. O'Shea, M. Reiser, and J. L. Vay. Collective space-charge phenomena in the source region. *Nuclear Inst. and Methods in Physics Research, A*, 519(1-2):396–404, 2004.

[52] Ronald C. Davidson, Hong Qin, Stephan I. Tzenov, and Edward A. Startsev. Kinetic description of intense beam propagation through a periodic focusing field for uniform phase-space density. *Phys. Rev. ST Accel. Beams*, 5(8):084402, Aug 2002.

[53] R. A. Kishek, P. G. O'Shea, M. Reiser, C. L. Bohn, I. Haber, and H. Kandrup. Computational investigation of dissipation and reversibility of space-charge driven processes in beams. In *Proceedings of the IEEE Particle Accelerator Conference (PAC 2001). 18-22 Jun 2001, Chicago, Illinois. 19th IEEE Particle Accelerator Conference, p.151-153*, pages 151–153, 2001.

[54] M. A. Holloway, R. B. Fiorito, A. G. Shkvarunets, P. G. O'Shea, S. V. Benson, D. Douglas, P. Evtushenko, and K. Jordan. Multicomponent measurements of the jefferson lab energy recovery linac electron beam using optical transition and diffraction radiation. *Phys. Rev. ST Accel. Beams*, 11(8):082801, Aug 2008.

[55] K. G. Sonnad and J. R. Cary. Halo mitigation using nonlinear lattices. In *Particle Accelerator Conference, 2005. PAC 2005. Proceedings of the*, pages 620–624, 2005.

[56] H. E. Kandrup, C. L. Bohn, R. A. Kishek, P. G. O'SHEA, M. Reiser, and I. V. Sideris. Chaotic collisionless evolution in galaxies and charged-particle beams. *Annals of the New York Academy of Sciences*, 1045(1 NONLINEAR DYNAMICS IN ASTRONOMY AND PHYSICS: In Memory of Henry E. Kandrup):12–33, 2005.

[57] D. Chernin. Evolution of rms beam envelopes in transport systems with linear $x - y$ coupling. *Particle Accelerators*, 24:29–44, 1988.

[58] J. J. Barnard. Emittance growth from rotated quadrupoles in heavy ion accelerators. In *Proceedings of the Particle Accelerator Conference, 1995*, volume 5, pages 3241–3244, May 1995.

[59] John J. Barnard and Bojan Losic. Enevelope modes of beams with angular momentum. In *XX International Linac Conference*, 2000.

[60] R. A. Kishek, J. J. Barnard, and D. P. Grote. Effects of quadrupole rotations on the transport of space-charge-dominated beams: theory and simulations comparing linacs with circular machines. In *Proceedings of the 1999 Particle Accelerator Conference, New York*, 1999.

[61] G. Franchetti and I. Hofmann. Space charge effect on emittance exchange by skew quadrupoles. In *Proceedings of the 1999 Particle Accelerator Conference, New York*, 1999.

[62] R. A. Kishek, S. Bernal, I. Haber, H. Li, P. G. O'Shea, B. Quinn, M. Reiser, and M. Walter. Beam halo from quadrupole rotation errors. In J. Wei, W. Fischer, and P. Manning, editors, *Beam-Halo Dynamics, Diagnositcs, and Collimation*, volume 693 of *American Institute of Physics Conference Series*, pages 89–92, dec 2003.

[63] Alex J. Dragt, Filippo Neri, and Govindan Rangarajan. General moment invariants for linear hamiltonian systems. *Phys. Rev. A*, 45(4):2572–2585, Feb 1992.

[64] Miguel A. Furman. Compact complex expressions for the electric field of two-dimensional elliptical charge distributions. *American Journal of Physics*, 62(12):1134–1140, 1994.

[65] R. B. Fiorito. Recent advances in OTR beam diagnostics. In *Proceedings of PAC09, Vancouver, BC*, 2009.

[66] J. Egberts, S. T. Artikova, and C. P. Welsch. Flexible core masking technique for beam halo measurements with high dynamic range. In *Proceedings of DIPAC09, Basel, Switzerland*, May 2009.

[67] Yan Levin, Renato Pakter, and Tarcisio N. Teles. Collisionless relaxation in non-neutral plasmas. *Physical Review Letters*, 100(4):040604, 2008.

[68] T. Padmanabhan. Statistical mechanics of gravitating systems. *PHYSICS REPORTS (Review Section of Physics Letters)*, 188(5):285–362, 1990.

[69] D. P. Grote, A. Friedman, and I. Haber. Methods used in WARP3d, a three-dimensional pic/accelerator code. In *Proc. of the 1996 Comp. Accel. Physics Conf.*, volume 391 of *AIP Conference Proceedings*, page 591, 1996.

[70] D. P. Grote, A. Friedman, J. L. Vay, and I. Haber. The warp code: modeling high intensity ion beams. *Electron Cyclotron Resonance Ion Sources*, 749:55–58, 2005.

[71] R. A. Kishek, P. G. O'Shea, and M. Reiser. Energy transfer in nonequilibrium space-charge-dominated beams. *Phys. Rev. Lett.*, 85(21):4514–4517, Nov 2000.